A hybrid fluid-kinetic model for hydrogenic atoms in the plasma edge of tokamaks based on a micro-macro decomposition of the kinetic equation

Niels Horsten[a,*], Giovanni Samaey[b], Martine Baelmans[a]

[a]*Department of Mechanical Engineering, KU Leuven, Celestijnenlaan 300, 3001 Leuven, Belgium*
[b]*Department of Computer Science, KU Leuven, Celestijnenlaan 200A, 3001 Leuven, Belgium*

Abstract

Monte Carlo (MC) simulations of the full kinetic equation for the neutral particles in the plasma edge become computationally costly for reactor-relevant regimes. To accelerate the simulations, we propose a hybrid fluid-kinetic approach that is based on a micro-macro decomposition of the kinetic equation. This leads to a macro/fluid model with kinetic corrections that follow from an MC simulation of the micro/kinetic part. We distinguish three hybrid models with different underlying fluid equations: (i) a pure pressure-diffusion equation with equal neutral and ion temperatures ($T_\mathrm{n} = T_\mathrm{i}$); (ii) a continuity and parallel momentum equation with pressure-diffusion transport retained in the directions perpendicular to the magnetic field lines, with $T_\mathrm{n} = T_\mathrm{i}$; and (iii) the same model as (ii), but with a separate neutral energy equation ($T_\mathrm{n} \neq T_\mathrm{i}$). To facilitate the future integration in more complete plasma edge codes, we neglect some kinetic correction terms. Hence, the hybrid model is not exactly equivalent to the full kinetic equation. We assess the hybrid performance on the basis of the reduction of the CPU time compared to an MC simulation of the full kinetic equation for the same statistical error on a certain plasma source. This is done for a high recycling slab case. Only the models with parallel momentum equation ((ii)-(iii)) are able to significantly reduce the CPU time. However, due to the incomplete kinetic corrections there is a remaining hybrid-kinetic discrepancy that mainly pops up in the ion energy source from the model with energy equation (iii).

1. Introduction

The plasma edge in magnetic confinement based nuclear fusion devices consists of plasma (mixture of ions and electrons) and neutral particles (atoms and molecules). The neutrals play a crucial role in reducing the particle and energy fluxes towards the divertor targets in the so-called detached operating regime. In this regime, a kind of

*Corresponding author: Tel.: +32 16 32 68 86;
Email address: niels.horsten@kuleuven.be (Niels Horsten)

neutral cushion in front of the divertor targets, with increased ion-neutral interactions, prevents a direct high-energetic plasma flow towards the targets. The detached regime is absolutely indispensable for large reactors as ITER and DEMO to keep the heat load below the maximum permitted value of 10 MW/m^2 [1]. Consequently, it is of crucial importance to accurately model the plasma and neutral species in the plasma edge for the development of operational scenarios and the design of future fusion reactors.

For the plasma species, one typically solves a set of Navier-Stokes like fluid equations, i.e., the Braginskii equations [2] supplemented with a model for anomalous transport perpendicular to the magnetic flux surfaces [3]. On the other hand, the neutral particles are usually described by means of a kinetic equation, which is an equation for the position-velocity phase-space distribution. The kinetic equation facilitates the incorporation of multiple kinds of advanced microscopic processes, such as the AMJUEL-HYDHEL databases [4, 5] for microscopic cross-sections and rate coefficients. Although deterministic approaches can be used to solve the plasma fluid equations, as implemented for example in the B2 and B2.5 finite-volume codes [6], such methods become computationally extremely costly for the kinetic neutral model due to the additional particle velocity dimensions. To cope with the high-dimensionality, a stochastic MC code is typically used, e.g., the EIRENE code [6], where an ensemble of particles is tracked from place of creation until absorption with a number of collisions on the particle trajectories.

The problems with the MC approach, in the way that it is for example implemented in the EIRENE code, are the fact that it hampers the convergence assessment when solving the coupled plasma-neutral equations [7] and the fact that it becomes computationally cumbersome for high-collisional cases, such as the (partially) detached regime. The latter issue originates from the fact that the full kinetic MC scheme is not asymptotic preserving [8], which means that the efficiency of the method strongly depends on the collisionality of the problem. Hence, a carefully designed (partially) deterministic neutral model can lead to a significant speed-up of plasma edge simulations.

For high-collisional cases, also the neutrals approach the fluid limit. Hence, as for the plasma, fluid equations can be solved for the neutrals, usually with a deterministic finite-volume approach. These approximate fluid neutral models tremendously accelerate the plasma edge simulations. In Ref. [9], we have assessed fluid models for the neutral atoms for a (partially) detached ITER case with fixed background plasma. Developing consistent fluid models for the molecules is still future research, since the molecule particle velocity distribution tends to strongly deviate from a Maxwellian equilibrium distribution. The use of fluid models for the atoms in Ref. [9] leads to plasma sources close to the target within 30% of accuracy compared to the kinetic solution. In the current paper, we go one step further by combining the fluid and kinetic approaches in a so-called hybrid fluid-kinetic model to resolve the remaining fluid-kinetic discrepancies, but with still a reduction of the computational time compared to the full kinetic MC solution for a given statistical error on a certain output of interest.

Hybrid fluid-kinetic methods are for example used in rarefied gas dynamics [10] and for neutron transport calculations [11]. The methods can be roughly subdivided in two categories: (i) domain decomposition methods, where the spatial domain consists of fluid and kinetic regions [12]; and (ii) full hybrid methods, where the particle population is split into a fluid and kinetic part [13]. A particularly beneficial property of a

certain (hybrid) scheme is that it is asymptotic preserving, where the scheme degenerates to a consistent discretization of the (fluid) limit equations when the collisionality becomes high. Most of the asymptotic-preserving methods in literature are based on fully deterministic grid-based schemes, see, e.g., Refs. [14, 15, 16, 17, 18, 19] and many others. In the particle setting, there are much less references for asymptotic-preserving schemes, e.g., Refs. [13, 20, 21, 22].

The first hybrid fluid-kinetic model for the neutrals in the plasma edge was theoretically elaborated in 1998 [23]. It is a full hybrid approach of type (ii) with interacting kinetic and fluid neutrals by means of fluid-kinetic transition sources/sinks. This hybrid approach is only recently implemented in the SOLEDGE2D-EIRENE code suite [24], where the magnitude of the fluid-kinetic transition sources is based on the local charge-exchange based Knudsen number. When using the hybrid method exclusively for the atoms (i.e., the molecules are still treated fully kinetically) for a high recycling ITER case, it leads to a reduction of approximately 10% for the EIRENE computational time compared to the full kinetic MC simulation with remaining hybrid-kinetic discrepancies on the plasma sources within 10%.

For the method of Refs. [23, 24], priori knowledge of the fluid and kinetic regions is needed to impose the transition sources. To avoid the need of fluid-kinetic detection criteria, we elaborate a hybrid approach based on a micro-macro decomposition of the kinetic equation. The micro-macro decomposition is, e.g., presented in Refs. [20, 25], where asymptotic-preserving schemes are obtained. Here, we apply the method specifically for the plasma edge neutrals, where the MC procedure differs from Refs. [20, 25] due to (i) the presence of sources and sinks, (ii) the dominance of neutral-ion charge-exchange scattering collisions instead of elastic self-collisions, and (iii) the fact that we use an MC procedure, which is particularly suitable for studying the neutral steady-state solution for a certain background plasma. Kinetic contributions appear in the fluid moment equations to correct for the closure approximations. For the micro-macro approach, there is no need for fluid-kinetic detection criteria, because the kinetic correction terms automatically vanish in the regions where the fluid limit is reached.

We have already applied the micro-macro hybrid approach to a 1D case with fixed background plasma that corresponds to the plasma results in a single flux tube from a 2D B2-EIRENE simulation on the ITER F12 geometry for a (partially) detached case [26]. In Ref. [27], we have reported that there is a reduction of the particle and momentum source statistical errors in that case with approximately a factor 5, and approximately a factor 3 for the ion energy source statistical error, compared to the full kinetic MC simulation for a given computational time.

In this paper, we extend the method for the 2D plasma edge. The plasma variables are kept fixed, i.e., the plasma equations are not solved. We provide a detailed algorithmic description of the method, using three different underlying fluid neutral models. The first fluid model consists of a pure pressure-diffusion equation, whereas the second model consists of a continuity and parallel momentum equation retaining pressure-diffusion transport in the directions perpendicular to the magnetic field. Both models assume that the ions and neutrals are at the same temperature, i.e., ion-neutral thermal equilibrium. This ion-neutral thermal equilibrium assumption disappears for the third model, where we solve a separate neutral energy equation. Preliminary nu-

merical results obtained with the first two models with ion-neutral thermal equilibrium assumption are already published in Ref. [28].

The paper is outlined as follows. In Section 2, we present the kinetic equation for the hydrogenic plasma edge atoms, for which we aim to develop a hybrid model. A hybrid approach for the molecules and other species is out of the scope of this paper, because of the lack of consistent fluid models for these species. In Section 3, we elaborate on the micro-macro decomposition of the kinetic (state) equation. The same micro-macro decomposition procedure is used for the boundary conditions in Section 4. Section 5 describes in detail the MC procedure for solving the micro equation, with main focus on the differences with the full kinetic MC procedure. In Section 6, we explain how the coupled fluid (macro)–kinetic (micro) neutral equations are solved. In Section 7, we compare the solutions from the different hybrid models with the kinetic and fluid solutions for a high recycling slab case. We evaluate the performance of the hybrid simulations on the basis of the reduction of the CPU time compared to the full kinetic MC solution for the same statistical error on a certain plasma source. Finally, Section 8 contains the conclusions and outlook for future work.

2. Kinetic equation

We only consider steady-state problems. The steady-state kinetic (Boltzmann) equation for the neutral atoms is

$$\mathbf{v} \cdot \nabla f_{\mathrm{n}}(\mathbf{r}, \mathbf{v}) = S\left(f_{\mathrm{n}}(\mathbf{r}, \mathbf{v})\right), \tag{1}$$

with $\mathbf{r} \in D \subset \mathbb{R}^2$ and $\mathbf{v} \in \mathbb{R}^3$ respectively the position and particle velocity vectors (D corresponds to the considered plasma edge domain, which is 2D due to the toroidal symmetry assumption), ∇ the gradient with respect to the position, $f_{\mathrm{n}}(\mathbf{r}, \mathbf{v})$ the position-velocity phase-space distribution and $S\left(f_{\mathrm{n}}(\mathbf{r}, \mathbf{v})\right)$ the term that contains all particle interactions (sources, sinks and scattering collisions). In this paper, we only consider deuterium atoms. However, the models from this paper can also be used for other hydrogen isotopes, because they undergo the same interactions. We take into account three processes: volumetric radiative recombination, electron impact ionization and charge-exchange collisions with respectively rate coefficients K_{r}, K_{i} and K_{cx}. The processes are sketched in Fig. 1, with e an electron, D a deuterium atom and D^+ a deuterium ion. From the neutral point of view, recombination is a source, ionization a sink and charge exchange a scattering event. The expressions for K_{r} and K_{i} as a function of the electron temperature can be found in Ref. [29, Section 10.3] and the expression for K_{cx} as a function of the ion temperature is taken from Ref. [30].

With these three processes, $S\left(f_{\mathrm{n}}(\mathbf{r}, \mathbf{v})\right)$ becomes

$$S\left(f_{\mathrm{n}}(\mathbf{r}, \mathbf{v})\right) = \widetilde{f_{\mathrm{i}}}(\mathbf{r}, \mathbf{v}) n_{\mathrm{i}}(\mathbf{r}) \left(n_{\mathrm{e}}(\mathbf{r}) K_{\mathrm{r}}(\mathbf{r}) + n_{\mathrm{n}}(\mathbf{r}) K_{\mathrm{cx}}(\mathbf{r})\right) - f_{\mathrm{n}}(\mathbf{r}, \mathbf{v}) R_{\mathrm{t}}(\mathbf{r}), \tag{2}$$

with $R_{\mathrm{t}}(\mathbf{r})$ the total collision rate of neutrals (i.e., ionization and charge exchange), given by

$$R_{\mathrm{t}}(\mathbf{r}) = n_{\mathrm{e}}(\mathbf{r}) K_{\mathrm{i}}(\mathbf{r}) + n_{\mathrm{i}}(\mathbf{r}) K_{\mathrm{cx}}(\mathbf{r}), \tag{3}$$

and $n_{\mathrm{i}}(\mathbf{r})$, $n_{\mathrm{e}}(\mathbf{r})$ and $n_{\mathrm{n}}(\mathbf{r}) = \int_{\mathbf{v}} f_{\mathrm{n}}(\mathbf{r}, \mathbf{v}) \mathrm{d}\mathbf{v}$ respectively the ion, electron and neutral density (number of particles per m^3), and $\widetilde{f_{\mathrm{i}}}(\mathbf{r}, \mathbf{v}) = f_{\mathrm{i}}(\mathbf{r}, \mathbf{v}) / n_{\mathrm{i}}(\mathbf{r})$ the normalized ion

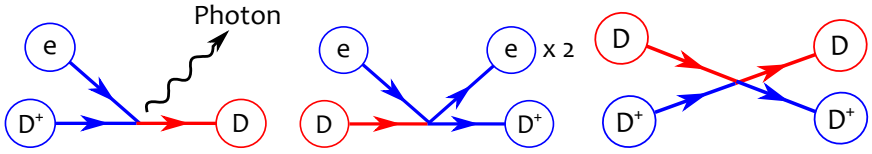

(a) Radiative recombination. (b) Electron impact ionization. (c) Charge-exchange collisions.

Figure 1: Processes for deuterium that we take into account.

distribution $\int_{\mathbf{v}} \widetilde{f}_{\mathrm{i}}(\mathbf{r},\mathbf{v})\mathrm{d}\mathbf{v} \equiv 1$. With $\int_{\mathbf{v}} \ldots \mathrm{d}\mathbf{v}$, we denote the integral over the whole velocity space for all velocity components from $-\infty$ to ∞. The spatial dependence of the rate coefficients follows from their temperature dependence, i.e., $K_{\mathrm{r}}(\mathbf{r}) \equiv K_{\mathrm{r}}(T_{\mathrm{e}}(\mathbf{r}))$, $K_{\mathrm{i}}(\mathbf{r}) \equiv K_{\mathrm{i}}(T_{\mathrm{e}}(\mathbf{r}))$ and $K_{\mathrm{cx}}(\mathbf{r}) \equiv K_{\mathrm{cx}}(T_{\mathrm{i}}(\mathbf{r}))$, with T_{e} and T_{i} respectively the electron and ion temperature. The neutral that results from a recombination or charge-exchange event gets the pre-collision ion velocity. This is the reason that the ion distribution appears in the recombination and charge-exchange terms from Eq. (2). Although, in fact, the ion distribution follows from the Braginskii approximation [2], which contains corrections on a perfect drifting Maxwellian distribution, it is nevertheless typical to assume a perfect drifting Maxwellian for the neutral simulations [31]. Then, the ion distribution is given by

$$\widetilde{f}_{\mathrm{i}}(\mathbf{r},\mathbf{v}) = \widetilde{M}(\mathbf{v};\mathbf{V}_{\mathrm{i}}(\mathbf{r}),T_{\mathrm{i}}(\mathbf{r})), \tag{4}$$

with

$$\widetilde{M}(\mathbf{v};\mathbf{V},T) = \left(\frac{m}{2\pi T}\right)^{3/2} \exp\left(-\frac{m}{2T}\|\mathbf{v}-\mathbf{V}\|^2\right), \tag{5}$$

with m the ion particle mass (or also the neutral atom mass, because we neglect the electron mass) and $\mathbf{V}_{\mathrm{i}}$ the ion fluid velocity vector. In this paper, temperatures are expressed in Joules. With $\|\ldots\|$, we denote the Euclidean norm. We assume that the ion fluid velocity is completely aligned to the magnetic field with parallel velocity component $u_{\parallel}$.

3. Micro-macro decomposition of the kinetic equation

The idea of the micro-macro decomposition is to write the neutral distribution as the sum of a fluid (macroscopic) part (subscript f) and kinetic (microscopic) part (subscript k):

$$f_{\mathrm{n}}(\mathbf{r},\mathbf{v}) = f_{\mathrm{n,f}}(\mathbf{r},\mathbf{v}) + f_{\mathrm{n,k}}(\mathbf{r},\mathbf{v}). \tag{6}$$

The fluid part is determined by solving a set of macroscopic fluid moment equations for the density, velocity and temperature (see Section 3.2). The errors made when closing the fluid equations are corrected by means of kinetic correction terms that follow from an MC simulation of the kinetic part (see Section 3.1). It is possible to use an arbitrary fluid distribution $f_{\mathrm{n,f}}(\mathbf{r},\mathbf{v})$ in Eq. (6), but the efficiency of the hybrid method strongly increases when using a fluid approximation that is already close to the total neutral distribution.

Such hybrid methods have been proposed, e.g., in Refs. [23, 24]. There, the distributions $f_{\mathrm{n,f}}(\mathbf{r},\mathbf{v})$ and $f_{\mathrm{n,k}}(\mathbf{r},\mathbf{v})$ are both positive for all $\mathbf{r} \in D$ and $\mathbf{v} \in \mathbb{R}^3$, which

implies that the fluid and kinetic parts can be considered as two physically meaningful interacting particle populations. In contrast, here, we impose the following condition:

$$n_{\mathrm{n}}(\mathbf{r}) = \int_{\mathbf{v}} f_{\mathrm{n}}(\mathbf{r},\mathbf{v})\mathrm{d}\mathbf{v} = \int_{\mathbf{v}} f_{\mathrm{n,f}}(\mathbf{r},\mathbf{v})\mathrm{d}\mathbf{v}, \tag{7}$$

which implies that all mass is contained in the fluid part of Eq. (6). The kinetic term in Eq. (6) then represents a correction with net zero mass at every location. This means that $f_{\mathrm{n,k}}(\mathbf{r},\mathbf{v})$ becomes negative for some values of $\mathbf{v}$ at every possible position $\mathbf{r}$.

In Section 3.1, we elaborate the micro model that determines $f_{\mathrm{n,k}}(\mathbf{r},\mathbf{v})$. The distribution $f_{\mathrm{n,f}}(\mathbf{r},\mathbf{v})$ follows from the solution of one of the fluid models from Section 3.2.

3.1. Micro/kinetic part

Inserting Eq. (6) in Eq. (1), gives

$$\mathbf{v}\cdot\nabla f_{\mathrm{n,k}}(\mathbf{r},\mathbf{v}) = S_{\mathrm{v}}(f_{\mathrm{n,f}}(\mathbf{r},\mathbf{v})) + \underbrace{\widetilde{f_{\mathrm{i}}}(\mathbf{r},\mathbf{v})n_{\mathrm{i}}(\mathbf{r})K_{\mathrm{cx}}(\mathbf{r})\int_{\mathbf{v}} f_{\mathrm{n,k}}(\mathbf{v})\mathrm{d}\mathbf{v}}_{\equiv 0} - R_{\mathrm{t}}(\mathbf{r})f_{\mathrm{n,k}}(\mathbf{r},\mathbf{v}), \tag{8}$$

with

$$S_{\mathrm{v}}(f_{\mathrm{n,f}}(\mathbf{r},\mathbf{v})) = -\mathbf{v}\cdot\nabla f_{\mathrm{n,f}}(\mathbf{r},\mathbf{v}) + S(f_{\mathrm{n,f}}(\mathbf{r},\mathbf{v})). \tag{9}$$

The left hand side of Eq. (8) corresponds to the transport of kinetic neutrals. The term $S_{\mathrm{v}}(f_{\mathrm{n,f}}(\mathbf{r},\mathbf{v}))$ represents the volumetric source of kinetic neutrals. In fact, the source is the residual of Eq. (1), when using the assumed fluid neutral distribution for the entire neutral population, and hence, the error of the fluid approximation on the kinetic level. Due to condition (7), the second term in the right hand side of Eq. (8) vanishes and the charge-exchange scattering character disappears from the kinetic equation. Consequently, there only remains absorption of kinetic neutrals with absorption rate R_{t}.

3.2. Macro/fluid part

The fluid distribution $f_{\mathrm{n,f}}(\mathbf{r},\mathbf{v})$, which is needed for solving the micro part (Eq. (8)), is uniquely determined by its corresponding macroscopic properties, which follow from the solution of a chosen fluid model. The fluid equations are obtained by taking moments of the kinetic equation. The zeroth, first and second order moment of Eq. (8) lead to the continuity, momentum and energy equations:

$$\int_{\mathbf{v}} \boldsymbol{\mu}(\mathbf{v})(\mathbf{v}\cdot\nabla f_{\mathrm{n,k}}(\mathbf{r},\mathbf{v}))\mathrm{d}\mathbf{v} = \int_{\mathbf{v}} \boldsymbol{\mu}(\mathbf{v})(S_{\mathrm{v}}(f_{\mathrm{n,f}}(\mathbf{r},\mathbf{v})) - R_{\mathrm{t}}(\mathbf{r})f_{\mathrm{n,k}}(\mathbf{r},\mathbf{v}))\mathrm{d}\mathbf{v}, \tag{10}$$

with

$$\boldsymbol{\mu}(\mathbf{v}) = \begin{bmatrix}\mu_1(\mathbf{v}) & \boldsymbol{\mu}_2^T(\mathbf{v}) & \mu_3(\mathbf{v})\end{bmatrix}^T, \quad \text{with} \quad \mu_1(\mathbf{v}) = 1, \;\; \boldsymbol{\mu}_2(\mathbf{v}) = m\mathbf{v}, \;\; \mu_3(\mathbf{v}) = m\|\mathbf{v}\|^2/2. \tag{11}$$

First, we elaborate the full continuity, momentum and energy equations. Subsequently, we reduce the models to obtain the fluid models from Ref. [9]. In this way, we show how the kinetic correction terms appear in the fluid equations. Although an arbitrary fluid model can be used, we will verify in Section 7.4 that the efficiency of the hybrid

approach strongly depends on the accuracy of the underlying fluid model. From now on, we omit the spatial dependence in the notation of the variables.

The continuity equation, i.e., the component for $\mu_1(\mathbf{v})$ in Eq. (10) (after rearranging the terms), becomes

$$\nabla \cdot \left(n_{\mathrm{n}} \mathbf{V}_{\mathrm{n,f}} + \int_{\mathbf{v}} \mathbf{v} f_{\mathrm{n,k}}(\mathbf{v}) \mathrm{d}\mathbf{v} \right) = -S_{n_{\mathrm{i}}}, \tag{12}$$

with the fluid momentum defined as $n_{\mathrm{n}} \mathbf{V}_{\mathrm{n,f}} \triangleq \int_{\mathbf{v}} \mathbf{v} f_{\mathrm{n,f}}(\mathbf{v}) \mathrm{d}\mathbf{v}$ and the plasma particle source $S_{n_{\mathrm{i}}} = -n_{\mathrm{i}} n_{\mathrm{e}} K_{\mathrm{r}} + n_{\mathrm{n}} n_{\mathrm{e}} K_{\mathrm{i}}$. For all upcoming fluid models, we impose that the macroscopic neutral particle flux follows entirely from the fluid distribution. This means that

$$n_{\mathrm{n}} \mathbf{V}_{\mathrm{n}} = \int_{\mathbf{v}} \mathbf{v} f_{\mathrm{n}}(\mathbf{v}) \mathrm{d}\mathbf{v} = \int_{\mathbf{v}} f_{\mathrm{n,f}}(\mathbf{v}) \mathrm{d}\mathbf{v} = n_{\mathrm{n}} \mathbf{V}_{\mathrm{n,f}}, \tag{13}$$

and $\int_{\mathbf{v}} \mathbf{v} f_{\mathrm{n,k}}(\mathbf{v}) \mathrm{d}\mathbf{v} \equiv 0$. With this condition, the continuity equation becomes

$$\nabla \cdot \mathbf{\Gamma}^{\mathrm{n}} = -S_{n_{\mathrm{i}}}, \tag{14}$$

with $\mathbf{\Gamma}^{\mathrm{n}}$ the neutral particle flux density vector, given by

$$\mathbf{\Gamma}^{\mathrm{n}} = n_{\mathrm{n}} \mathbf{V}_{\mathrm{n}}. \tag{15}$$

The momentum (vector) equation ($\boldsymbol{\mu}_2(\mathbf{v})$ in Eq. (10)) becomes

$$\nabla \cdot \Gamma_{\mathrm{m}}^{\mathrm{n}} = -\mathbf{S}_{m\mathbf{V}_{\mathrm{i}}}, \tag{16}$$

with $\Gamma_{\mathrm{m}}^{\mathrm{n}}$ the momentum flux density tensor, given by

$$\Gamma_{\mathrm{m}}^{\mathrm{n}} = m n_{\mathrm{n}} \mathbf{V}_{\mathrm{n}} \mathbf{V}_{\mathrm{n}} + p_{\mathrm{n,f}} \mathbb{I} + p_{\mathrm{n,k}} \mathbb{I} + \Pi_{\mathrm{n,f}} + \Pi_{\mathrm{n,k}}, \tag{17}$$

with $\mathbb{I}$ the identity tensor, and the fluid pressure $p_{\mathrm{n,f}}$ and fluid stress tensor $\Pi_{\mathrm{n,f}}$ defined as

$$p_{\mathrm{n,f}} \triangleq \frac{m}{3} \int_{\mathbf{v}} \|\mathbf{v} - \mathbf{V}_{\mathrm{n}}\|^2 f_{\mathrm{n,f}}(\mathbf{v}) \mathrm{d}\mathbf{v}, \qquad \Pi_{\mathrm{n,f}} \triangleq m \int_{\mathbf{v}} (\mathbf{v} - \mathbf{V}_{\mathrm{n}})(\mathbf{v} - \mathbf{V}_{\mathrm{n}}) f_{\mathrm{n,f}}(\mathbf{v}) \mathrm{d}\mathbf{v} - p_{\mathrm{n,f}} \mathbb{I}. \tag{18}$$

The kinetic pressure $p_{\mathrm{n,k}}$ and kinetic stress tensor $\Pi_{\mathrm{n,k}}$ are defined as

$$p_{\mathrm{n,k}} \triangleq \frac{m}{3} \int_{\mathbf{v}} \|\mathbf{v}\|^2 f_{\mathrm{n,k}}(\mathbf{v}) \mathrm{d}\mathbf{v}, \qquad \Pi_{\mathrm{n,k}} \triangleq m \int_{\mathbf{v}} \mathbf{v}\mathbf{v} f_{\mathrm{n,k}}(\mathbf{v}) \mathrm{d}\mathbf{v} - p_{\mathrm{n,k}} \mathbb{I}. \tag{19}$$

It should be noted that for the kinetic contributions (Eq. (19)) the total second order moment is taken instead of the moment with the peculiar velocity for the fluid contributions ($\mathbf{v} - \mathbf{V}_{\mathrm{n}}$ in Eq. (18)). Doing so is valid due to the assumption of zero kinetic particle flux (Eq. (13)). The momentum source term becomes

$$\mathbf{S}_{m\mathbf{V}_{\mathrm{i}}} = -m n_{\mathrm{i}} (n_{\mathrm{e}} K_{\mathrm{r}} + n_{\mathrm{n}} K_{\mathrm{cx}}) \mathbf{V}_{\mathrm{i}} + m n_{\mathrm{n}} (n_{\mathrm{e}} K_{\mathrm{i}} + n_{\mathrm{i}} K_{\mathrm{cx}}) \mathbf{V}_{\mathrm{n}}. \tag{20}$$

We use $\Gamma_{\mathrm{m}}^{\mathrm{n}}$ for the neutral momentum flux density tensor, defined in Eq. (16).

Finally, the energy equation ($\mu_3(\mathbf{v})$ in Eq. (10)) becomes

$$\nabla \cdot \mathbf{Q}^{\mathrm{n}} = -S_{E_{\mathrm{i}}}, \tag{21}$$

with $\mathbf{Q}^{\mathrm{n}}$ the energy flux density vector, given by

$$\mathbf{Q}^{\mathrm{n}} = \left(\frac{5}{2}p_{\mathrm{n,f}} + \frac{m}{2}n_{\mathrm{n}}\|\mathbf{V}_{\mathrm{n}}\|^2\right)\mathbf{V}_{\mathrm{n}} + \Pi_{\mathrm{n,f}} \cdot \mathbf{V}_{\mathrm{n}} + \mathbf{q}_{\mathrm{n,f}} + \mathbf{q}_{\mathrm{n,k}}, \tag{22}$$

with the fluid and kinetic heat flux vectors defined as

$$\mathbf{q}_{\mathrm{n,f}} \triangleq \frac{m}{2}\int_{\mathbf{v}} \|\mathbf{v} - \mathbf{V}_{\mathrm{n}}\|^2(\mathbf{v} - \mathbf{V}_{\mathrm{n}})f_{\mathrm{n,f}}(\mathbf{v})\mathrm{d}\mathbf{v}, \qquad \mathbf{q}_{\mathrm{n,k}} \triangleq \frac{m}{2}\int_{\mathbf{v}} \|\mathbf{v}\|^2\mathbf{v}f_{\mathrm{n,k}}(\mathbf{v})\mathrm{d}\mathbf{v}, \tag{23}$$

where again the total moment is taken for the kinetic heat flux vector. The energy source becomes

$$S_{E_{\mathrm{i}}} = -n_{\mathrm{i}}(n_{\mathrm{e}}K_{\mathrm{r}} + n_{\mathrm{n}}K_{\mathrm{cx}})\left(\frac{3}{2}T_{\mathrm{i}} + \frac{m}{2}\|\mathbf{V}_{\mathrm{i}}\|^2\right) + (n_{\mathrm{e}}K_{\mathrm{i}} + n_{\mathrm{i}}K_{\mathrm{cx}})\left(\frac{3}{2}p_{\mathrm{n,f}} + \frac{3}{2}p_{\mathrm{n,k}} + \frac{m}{2}n_{\mathrm{n}}\|\mathbf{V}_{\mathrm{n}}\|^2\right). \tag{24}$$

The neutral energy flux density vector is indicated with $\mathbf{Q}^{\mathrm{n}}$, see Eq. (21).

Now, we have obtained all moment equations with kinetic correction contributions, i.e., the continuity (Eq. (14)), momentum (Eq. (16)) and energy (Eq. (21)) equations. We notice that kinetic correction terms appear in these equations, i.e., $p_{\mathrm{n,k}}$ and $\Pi_{\mathrm{n,k}}$ in Eq. (16) and $\mathbf{q}_{\mathrm{n,k}}$ in Eq. (21). These kinetic contributions follow from an MC simulation of the micro part (Eq. (8)), as will be explained in Section 5. Besides that, the moment equations are not closed due to the presence of the unknown fluid viscosity tensor $\Pi_{\mathrm{n,f}}$ and heat flux vector $\mathbf{q}_{\mathrm{n,f}}$. In the following subsections, we elaborate the three fluid closure approximations from Ref. [9]. The first model (Section 3.2.1) consists of a pure pressure-diffusion equation with ion-neutral thermal equilibrium assumption. The second model (Section 3.2.2) consists of a continuity and parallel momentum equation retaining the pressure-diffusion transport in the directions perpendicular to the magnetic field. We still assume ion-neutral thermal equilibrium. The last model (Section 3.2.3) is similar as the second model, but we add a separate neutral energy equation, i.e., it is no longer assumed that the ions and neutrals are at the same temperature.

3.2.1. Model 1: pressure-diffusion equation

If the convective and viscous (fluid) transport in the momentum equation (Eq. (16)) is neglected, we obtain immediately an expression for the neutral particle flux density:

$$\mathbf{\Gamma}^{\mathrm{n}} = n_{\mathrm{n}}\mathbf{V}_{\mathrm{n}} = n_{\mathrm{n,eq}}\mathbf{V}_{\mathrm{i}} - D_p^{\mathrm{n}}\nabla p_{\mathrm{n,f}} - D_p^{\mathrm{n}}\nabla p_{\mathrm{n,k}} - D_p^{\mathrm{n}}\nabla \cdot \Pi_{\mathrm{n,k}}, \tag{25}$$

with $n_{\mathrm{n,eq}} = (n_{\mathrm{i}}n_{\mathrm{e}}K_{\mathrm{r}} + n_{\mathrm{n}}n_{\mathrm{i}}K_{\mathrm{cx}})/(n_{\mathrm{i}}K_{\mathrm{cx}} + n_{\mathrm{e}}K_{\mathrm{i}})$ and the pressure-diffusion coefficient $D_p^{\mathrm{n}} = (m(n_{\mathrm{i}}K_{\mathrm{cx}} + n_{\mathrm{e}}K_{\mathrm{i}}))^{-1}$. Inserting Eq. (25) in the continuity equation (Eq. (14)) leads to the so-called pressure-diffusion equation:

$$\nabla \cdot (n_{\mathrm{n,eq}}\mathbf{V}_{\mathrm{i}} - D_p^{\mathrm{n}}\nabla p_{\mathrm{n,f}} - D_p^{\mathrm{n}}\nabla p_{\mathrm{n,k}} - D_p^{\mathrm{n}}\nabla \cdot \Pi_{\mathrm{n,k}}) = -S_{n_{\mathrm{i}}}. \tag{26}$$

Eq. (26) is a single convection-diffusion equation that is solved for the fluid neutral pressure $p_{\mathrm{n,f}}$. The neutral density follows from the ideal gas law where we assume ion-neutral thermal equilibrium, i.e., $p_{\mathrm{n,f}} = n_{\mathrm{n}}T_{\mathrm{i}}$.

3.2.2. Model 2: continuity and parallel momentum equation

For the second model, we solve the continuity equation (Eq. (14)) together with the component of the momentum equation (Eq. (16)) parallel to the magnetic field. For the expression of the fluid stress tensor, we use Chapman-Enskog's closure method [32] (based on the charge-exchange collision frequency). This gives

$$\Pi_{\mathrm{n,f}} = -\eta^{\mathrm{n}} \left(\nabla \mathbf{V}_{\mathrm{n}} + (\nabla \mathbf{V}_{\mathrm{n}})^T - \frac{2}{3} (\nabla \cdot \mathbf{V}_{\mathrm{n}}) \mathbb{I} \right), \tag{27}$$

with the viscosity $\eta^{\mathrm{n}} = p_{\mathrm{n,f}}/(n_{\mathrm{i}} K_{\mathrm{cx}})$. Only the expected relevant curvilinear effects for a dominant flow in the parallel direction are taken into account [9]. Then, the parallel momentum equation (solved for the neutral parallel velocity $u_{\mathrm{n}\parallel}$) becomes

$$\frac{1}{R} \nabla \cdot \left(R \left(m n_{\mathrm{n}} u_{\mathrm{n}\parallel} \mathbf{V}_{\mathrm{n}} - \eta^{\mathrm{n}} \left(\nabla u_{\mathrm{n}\parallel} - u_{\mathrm{n}\parallel} \frac{1}{R} \nabla R \right) \right) \right) = -\nabla_{\parallel} p_{\mathrm{n,f}} - \nabla_{\parallel} p_{\mathrm{n,k}} - \left[\nabla \cdot \Pi_{\mathrm{n,k}} \right]_{\parallel} - S_{mu_{\parallel}}, \tag{28}$$

with R the local value of the major radius, the subscript $\parallel$ indicating the parallel component of a vector, and the parallel momentum source $S_{mu_{\parallel}}$, given by

$$S_{mu_{\parallel}} = -m n_{\mathrm{i}} (n_{\mathrm{e}} K_{\mathrm{r}} + n_{\mathrm{n}} K_{\mathrm{cx}}) u_{\parallel} + m n_{\mathrm{n}} (n_{\mathrm{e}} K_{\mathrm{i}} + n_{\mathrm{i}} K_{\mathrm{cx}}) u_{\mathrm{n}\parallel}. \tag{29}$$

The neutral transport perpendicular to the magnetic field (the so-called radial and diamagnetic directions) is still governed by the pressure-diffusion law:

$$[n_{\mathrm{n}} \mathbf{V}_{\mathrm{n}}]_{r,\perp} = \left[-D_p^{\mathrm{n}} \nabla p_{\mathrm{n,f}} - D_p^{\mathrm{n}} \nabla p_{\mathrm{n,k}} - D_p^{\mathrm{n}} \nabla \cdot \Pi_{\mathrm{n,k}} \right]_{r,\perp}, \tag{30}$$

with the subscripts r and $\perp$ for respectively the radial and diamagnetic components. Again, we still assume that $p_{\mathrm{n,f}} = n_{\mathrm{n}} T_{\mathrm{i}}$.

3.2.3. Model 3: continuity, parallel momentum and energy equation

For the last model, we again solve the continuity equation (Eq. (14)) with parallel momentum equation (Eq. (28)), with pressure-diffusion transport perpendicular to the magnetic field (Eq. (30)). However, we no longer assume ion-neutral thermal equilibrium. Then, the fluid pressure becomes $p_{\mathrm{n,f}} = n_{\mathrm{n}} T_{\mathrm{n}}$, with T_{n} the solution of the neutral energy equation. Again, the Chapman-Enskog procedure is used for the fluid heat flux vector. This gives

$$\mathbf{q}_{\mathrm{n,f}} = -\kappa^{\mathrm{n}} \nabla T_{\mathrm{n}}, \tag{31}$$

with the heat conduction coefficient $\kappa^{\mathrm{n}} = 5 n_{\mathrm{n}} T_{\mathrm{n}}/(2 m n_{\mathrm{i}} K_{\mathrm{cx}})$. Then, the energy equation (Eq. (21)), with the assumption of dominant neutral fluid velocity parallel to the magnetic field, becomes

$$\nabla \cdot \left(\left(\frac{5}{2} T_{\mathrm{n}} + \frac{m}{2} u_{\mathrm{n}\parallel}^2 \right) n_{\mathrm{n}} \mathbf{V}_{\mathrm{n}} - \frac{\eta^{\mathrm{n}}}{2} \nabla \left(u_{\mathrm{n}\parallel}^2 \right) + \eta^{\mathrm{n}} u_{\mathrm{n}\parallel}^2 \frac{1}{R} \nabla R - \kappa^{\mathrm{n}} \nabla T_{\mathrm{n}} + \mathbf{q}_{\mathrm{n,k}} \right) = -S_{E_{\mathrm{i}}}. \tag{32}$$

It should be noted that for this last model $p_{\mathrm{n,k}} \equiv 0$, due to the fact that the fluid pressure corresponds to the total population, i.e.,

$$p_{\mathrm{n,f}} = \frac{m}{3} \int_{\mathbf{v}} \| \mathbf{v} - \mathbf{V}_{\mathrm{n}} \|^2 f_{\mathrm{n}}(\mathbf{v}) \mathrm{d}\mathbf{v}. \tag{33}$$

3.2.4. Fluid neutral velocity distribution

To solve the micro equation (Eq. (8)), we need an expression for $f_{\mathrm{n,f}}(\mathbf{r}, \mathbf{v})$. In fact, this fluid distribution depends on the chosen fluid model. However, this distribution might become complicated, which makes the future integration in a more complete plasma edge code suite difficult, as e.g., SOLPS-ITER [33]. Additionally, it is not sure that there always exists a distribution [34]. Therefore, we assume that the fluid neutral distribution corresponds to a perfect drifting Maxwellian for all fluid models, i.e.,

$$f_{\mathrm{n,f}}(\mathbf{r}, \mathbf{v}) = n_{\mathrm{n}}(\mathbf{r})\widetilde{M}(\mathbf{v}; \mathbf{V}_{\mathrm{n}}(\mathbf{r}), T_{\mathrm{n,f}}(\mathbf{r})), \tag{34}$$

with $T_{\mathrm{n,f}} = p_{\mathrm{n,f}}/n_{\mathrm{n}}$ the neutral fluid temperature. In practice, $f_{\mathrm{n,f}}(\mathbf{r}, \mathbf{v})$ deviates from a perfect drifting Maxwellian due to the fact that some terms are neglected in the fluid moment equations (e.g., the convective momentum transport for the pressure-diffusion approach) and the possible presence of viscous momentum transport and conductive heat losses in the fluid equations. Hence, the perfect drifting Maxwellian assumption is a zeroth order approximation of the complete Chapman-Enskog fluid distribution.

Summarized, we now have obtained a micro equation (Eq. (8)) with contributions from the fluid neutrals in the density n_{n} and distribution $f_{\mathrm{n,f}}(\mathbf{v})$. These fluid properties follow from one of the macro/fluid models (Sections 3.2.1-3.2.3). However, in these fluid equations, at their turn, kinetic correction terms appear (kinetic pressure, stress tensor and heat flux vector). These kinetic corrections are specific moments of the kinetic distribution. This means that we have obtained a set of coupled kinetic (micro) and fluid (macro) equations. In the next section, we define the boundary conditions.

4. Micro-macro decomposition of the boundary conditions

In this section, we repeat the same micro-macro decomposition procedure for the boundary conditions. First, we present the boundary condition of the full kinetic equation (Eq. (1)) in Section 4.1. Subsequently, we perform the micro-macro decomposition to obtain boundary conditions for the micro equation (Eq. (8)) in Section 4.2 and for the macro models (Sections 3.2.1-3.2.3) in Section 4.3.

4.1. Kinetic boundary condition

The emitted neutral particle flux at a certain boundary point consists of a recycled and reflected part. With the recycled part, we mean the fraction due to the recombination of ions and electrons at the surface. The recycling coefficient $R^{\mathrm{i}}(\mathbf{r}_{\mathrm{b}})$ (with $\mathbf{r}_{\mathrm{b}}$ a point at the boundary, i.e., $\mathbf{r}_{\mathrm{b}} \in \partial D$) gives the probability that the particle is recycled, hence, $1 - R^{\mathrm{i}}(\mathbf{r}_{\mathrm{b}})$ of the incident plasma is absorbed at location $\mathbf{r}_{\mathrm{b}}$. The distribution of the incident ions is $f_{\mathrm{i,b}}(\mathbf{r}_{\mathrm{b}}, \mathbf{v}')$, which is a truncated Maxwellian ($f_{\mathrm{i,b}}(\mathbf{r}_{\mathrm{b}}, \mathbf{v}') \equiv 0, \ \forall \mathbf{v}' \cdot \boldsymbol{\nu}(\mathbf{r}_{\mathrm{b}}) > 0$, with $\boldsymbol{\nu}(\mathbf{r}_{\mathrm{b}})$ the surface normal unit vector pointing inward the plasma region) possibly accelerated by the sheath potential if the magnetic field is not perfectly aligned to the boundary surface [35]. Besides the incident plasma, there are also incident neutrals that are reflected (with probability $R^{\mathrm{n}}(\mathbf{r}_{\mathrm{b}})$). Finally, the reflection kernel $R(\mathbf{r}_{\mathrm{b}}; \mathbf{v}' \rightarrow \mathbf{v})$ gives the velocity distribution of the recycled/reflected particles if the incident particle velocity is $\mathbf{v}'$. Because the recycling/reflection probability is already contained in

$R^{\mathrm{i}}(\mathbf{r}_\mathrm{b})$ and $R^{\mathrm{n}}(\mathbf{r}_\mathrm{b})$, we know that $\int_{\mathbf{v}\cdot\boldsymbol{\nu}(\mathbf{r}_\mathrm{b})>0} R(\mathbf{r}_\mathrm{b};\mathbf{v}'\to\mathbf{v})\mathrm{d}\mathbf{v} = 1$, with $\int_{\mathbf{v}\cdot\boldsymbol{\nu}(\mathbf{r}_\mathrm{b})>0}\ldots\mathrm{d}\mathbf{v}$ the integral over $\{\mathbf{v}\in\mathbb{R}^3|\mathbf{v}\cdot\boldsymbol{\nu}(\mathbf{r}_\mathrm{b})>0\}$.

Then, the kinetic boundary condition becomes

$$f_{\mathrm{n}}(\mathbf{r}_\mathrm{b},\mathbf{v})(\mathbf{v}\cdot\boldsymbol{\nu}(\mathbf{r}_\mathrm{b})) = -\int_{\mathbf{v}'\cdot\boldsymbol{\nu}(\mathbf{r}_\mathrm{b})<0} R(\mathbf{r}_\mathrm{b};\mathbf{v}'\to\mathbf{v})(\underbrace{R^{\mathrm{i}}(\mathbf{r}_\mathrm{b})f_{\mathrm{i,b}}(\mathbf{r}_\mathrm{b},\mathbf{v}')}_{\text{recycled}} + \underbrace{R^{\mathrm{n}}(\mathbf{r}_\mathrm{b})f_{\mathrm{n}}(\mathbf{r}_\mathrm{b},\mathbf{v}')}_{\text{reflected}})(\mathbf{v}'\cdot\boldsymbol{\nu}(\mathbf{r}_\mathrm{b}))\mathrm{d}\mathbf{v}', \quad \text{for} \quad \mathbf{v}\cdot\boldsymbol{\nu}(\mathbf{r}_\mathrm{b})>0,\ \ \mathbf{r}_\mathrm{b}\in\partial D, \quad (35)$$

with $\int_{\mathbf{v}'\cdot\boldsymbol{\nu}(\mathbf{r}_\mathrm{b})<0}\ldots\mathrm{d}\mathbf{v}'$ the integral over $\{\mathbf{v}'\in\mathbb{R}^3|\mathbf{v}'\cdot\boldsymbol{\nu}(\mathbf{r}_\mathrm{b})<0\}$.

Now, we also apply the micro-macro decomposition to the boundary condition.

4.2. Micro/kinetic part

Inserting Eq. (6) in Eq. (35) and rearranging the terms, gives

$$f_{\mathrm{n,k}}(\mathbf{r}_\mathrm{b},\mathbf{v})(\mathbf{v}\cdot\boldsymbol{\nu}(\mathbf{r}_\mathrm{b})) = -S_\mathrm{b}^-(\mathbf{r}_\mathrm{b},\mathbf{v}) + S_\mathrm{b}^+(\mathbf{r}_\mathrm{b},\mathbf{v}) - \int_{\mathbf{v}'\cdot\boldsymbol{\nu}(\mathbf{r}_\mathrm{b})<0} R(\mathbf{r}_\mathrm{b};\mathbf{v}'\to\mathbf{v})R^{\mathrm{n}}(\mathbf{r}_\mathrm{b})f_{\mathrm{n,k}}(\mathbf{r}_\mathrm{b},\mathbf{v}')(\mathbf{v}'\cdot\boldsymbol{\nu}(\mathbf{r}_\mathrm{b}))\mathrm{d}\mathbf{v}', \quad \text{for} \quad \mathbf{v}\cdot\boldsymbol{\nu}(\mathbf{r}_\mathrm{b})>0,\ \ \mathbf{r}_\mathrm{b}\in\partial D, \quad (36)$$

with $S_\mathrm{b}^-(\mathbf{r}_\mathrm{b},\mathbf{v})$ and $S_\mathrm{b}^+(\mathbf{r}_\mathrm{b},\mathbf{v})$ the kinetic surface sources arising from the fluid part of the distribution, given by

$$S_\mathrm{b}^-(\mathbf{r}_\mathrm{b},\mathbf{v}) = f_{\mathrm{n,f}}(\mathbf{r}_\mathrm{b},\mathbf{v})(\mathbf{v}\cdot\boldsymbol{\nu}(\mathbf{r}_\mathrm{b})), \quad (37)$$

$$S_\mathrm{b}^+(\mathbf{r}_\mathrm{b},\mathbf{v}) = -\int_{\mathbf{v}'\cdot\boldsymbol{\nu}(\mathbf{r}_\mathrm{b})<0} R(\mathbf{r}_\mathrm{b};\mathbf{v}'\to\mathbf{v})(R^{\mathrm{i}}(\mathbf{r}_\mathrm{b})f_{\mathrm{i,b}}(\mathbf{r}_\mathrm{b},\mathbf{v}') + R^{\mathrm{n}}(\mathbf{r}_\mathrm{b})f_{\mathrm{n,f}}(\mathbf{r}_\mathrm{b},\mathbf{v}'))(\mathbf{v}'\cdot\boldsymbol{\nu}(\mathbf{r}_\mathrm{b}))\mathrm{d}\mathbf{v}' \quad (38)$$

The last term of Eq. (36) corresponds to the reflection of kinetic neutrals.

4.3. Macro/fluid part

For the macro/fluid equations, we impose boundary fluxes, i.e., particle, momentum and energy fluxes for the corresponding equations. These boundary fluxes follow from the particular moments of Eq. (36):

$$\begin{aligned}\boldsymbol{\Gamma}_\mu^{\mathrm{n}}(\mathbf{r}_\mathrm{b}) &= \begin{bmatrix}\Gamma^{\mathrm{n}}(\mathbf{r}_\mathrm{b}) & (\boldsymbol{\Gamma}_{\mathrm{m}}^{\mathrm{n}}(\mathbf{r}_\mathrm{b}))^T & Q^{\mathrm{n}}(\mathbf{r}_\mathrm{b})\end{bmatrix}^T \\ &= \underbrace{\int_{\mathbf{v}'\cdot\boldsymbol{\nu}(\mathbf{r}_\mathrm{b})<0}\boldsymbol{\mu}(\mathbf{v}')f_{\mathrm{n,f}}(\mathbf{r}_\mathrm{b},\mathbf{v}')(\mathbf{v}'\cdot\boldsymbol{\nu}(\mathbf{r}_\mathrm{b}))\mathrm{d}\mathbf{v}'}_{\text{incident fluid neutrals}} \\ &\quad \underbrace{-\int_{\mathbf{v}\cdot\boldsymbol{\nu}(\mathbf{r}_\mathrm{b})>0}\boldsymbol{\mu}(\mathbf{v})\left(\int_{\mathbf{v}'\cdot\boldsymbol{\nu}(\mathbf{r}_\mathrm{b})<0} R(\mathbf{r}_\mathrm{b};\mathbf{v}'\to\mathbf{v})(R^{\mathrm{i}}(\mathbf{r}_\mathrm{b})f_{\mathrm{i,b}}(\mathbf{r}_\mathrm{b},\mathbf{v}') + R^{\mathrm{n}}(\mathbf{r}_\mathrm{b})f_{\mathrm{n,f}}(\mathbf{r}_\mathrm{b},\mathbf{v}'))(\mathbf{v}'\cdot\boldsymbol{\nu}(\mathbf{r}_\mathrm{b}))\mathrm{d}\mathbf{v}'\right)\mathrm{d}\mathbf{v}}_{\text{recycled/reflected fluid neutrals}} \\ &\quad +\boldsymbol{\Gamma}_{\mu,\mathrm{k}}^{\mathrm{n}}(\mathbf{r}_\mathrm{b}), \end{aligned} \quad (39)$$

with $\boldsymbol{\mu}(\mathbf{v})$ defined in Eq. (11), $\Gamma^{\mathrm{n}}(\mathbf{r}_{\mathrm{b}}) = \boldsymbol{\Gamma}^{\mathrm{n}}(\mathbf{r}_{\mathrm{b}}) \cdot \boldsymbol{\nu}(\mathbf{r}_{\mathrm{b}})$, $\Gamma^{\mathrm{n}}_{\mathrm{m}}(\mathbf{r}_{\mathrm{b}}) = \boldsymbol{\Gamma}^{\mathrm{n}}_{\mathrm{m}}(\mathbf{r}_{\mathrm{b}}) \cdot \boldsymbol{\nu}(\mathbf{r}_{\mathrm{b}})$ and $Q^{\mathrm{n}}(\mathbf{r}_{\mathrm{b}}) = \mathbf{Q}^{\mathrm{n}}(\mathbf{r}_{\mathrm{b}}) \cdot \boldsymbol{\nu}(\mathbf{r}_{\mathrm{b}})$ respectively the particle, momentum and energy flux density (with $\boldsymbol{\Gamma}^{\mathrm{n}}$, $\boldsymbol{\Gamma}^{\mathrm{n}}_{\mathrm{m}}$ and $\mathbf{Q}^{\mathrm{n}}$ defined in Eqs. (14)-(16),(21)), and

$$\begin{aligned}\boldsymbol{\Gamma}^{\mathrm{n}}_{\mu,\mathrm{k}}(\mathbf{r}_{\mathrm{b}}) \quad = \quad & \underbrace{\int_{\mathbf{v}'\cdot\boldsymbol{\nu}(\mathbf{r}_{\mathrm{b}})<0} \boldsymbol{\mu}(\mathbf{v}') f_{\mathrm{n,k}}(\mathbf{r}_{\mathrm{b}}, \mathbf{v}')(\mathbf{v}' \cdot \boldsymbol{\nu}(\mathbf{r}_{\mathrm{b}}))\mathrm{d}\mathbf{v}'}_{\text{incident kinetic neutrals}} \\ & \underbrace{-R^{\mathrm{n}}(\mathbf{r}_{\mathrm{b}}) \int_{\mathbf{v}\cdot\boldsymbol{\nu}(\mathbf{r}_{\mathrm{b}})>0} \boldsymbol{\mu}(\mathbf{v}) \left(\int_{\mathbf{v}'\cdot\boldsymbol{\nu}(\mathbf{r}_{\mathrm{b}})<0} R(\mathbf{r}_{\mathrm{b}}; \mathbf{v}' \rightarrow \mathbf{v}) f_{\mathrm{n,k}}(\mathbf{r}_{\mathrm{b}}, \mathbf{v}')(\mathbf{v}' \cdot \boldsymbol{\nu}(\mathbf{r}_{\mathrm{b}}))\mathrm{d}\mathbf{v}' \right) \mathrm{d}\mathbf{v}}_{\text{reflected kinetic neutrals}} \end{aligned} \tag{40}$$

the kinetic corrections in the fluid boundary conditions. The particle flux density is imposed for the continuity and pressure-diffusion equation (respectively Eq. (14) and Eq. (26)), the parallel component of the momentum flux density for the parallel momentum equation (Eq. (28)), and the energy flux density for the energy equation (Eq. (32)).

With the definition of micro and macro boundary conditions, we have obtained a closed micro-macro model that can be solved. Section 5 deals with the MC simulation for the micro part and Section 6 discusses the global solution procedure for the system of coupled fluid-kinetic equations.

5. Monte Carlo simulation of the kinetic part

The MC procedure, as implemented in the EIRENE code [31], exploits the linearity of the Boltzmann equation (Eq. (1)) due to the fact that the neutral particles only interact with the plasma background, which can be considered as fixed from the neutral point of view. Therefore, the neutral paths are treated as independent non-interacting trajectories and the code can be easily parallellized. The default EIRENE analog simulation of an individual particle trajectory consists of the following steps: 1) sample the initial position and velocity based on the source distributions (in the volume or at the boundary surface), 2) calculate the particle trajectory until the next event (a collision in the domain or at a boundary surface), 3) determine if the particle is absorbed, and 4) if the particle is not absorbed, re-sample the velocity and go back to step 2, otherwise, the trajectory is ended. This process is repeated (possibly in parallel) for the total amount of particles N.

Each particle has a weight w, which can vary on the particle trajectory. This weight determines how much the particle contributes to the estimates of the outputs of interest, which are called tallies in MC terminology, see Section 5.4. With analog simulation, we mean that the particle is launched with initial weight w_0 and this weight does not alter on the particle trajectory. At a collision event at location $\mathbf{r}$, the particle is absorbed with probability $R_{\mathrm{a}}(\mathbf{r})/R_{\mathrm{t}}(\mathbf{r})$, with $R_{\mathrm{a}}(\mathbf{r})$ and $R_{\mathrm{t}}(\mathbf{r})$ respecitvely the absorption and total reaction rate. The initial weights are mostly one, except when importance sampling [36] is used. For the latter technique, the particle position and velocity are sampled from an alternative distribution and the particle gets the ratio of the original and sampled distribution as initial weight. Besides the analog simulation, it is also

possible to, e.g., rescale the particle weight on its trajectory to account for absorption events, instead of immediately ending the particle trajectory. See, e.g., Ref. [37] for an overview of different simulation strategies.

The same steps can be found in the MC procedure for the micro equation in the hybrid model (Eq. (8) with boundary condition (36)). However, there are significant differences that we highlight in this section.

The total position- and velocity-dependent source $S_{\mathrm{k}}(\mathbf{r}, \mathbf{v})$ for the micro equation can be written as

$$S_{\mathrm{k}}(\mathbf{r}, \mathbf{v}) = S_{\mathrm{v}}(f_{\mathrm{n,f}}(\mathbf{r}, \mathbf{v})) + (S_{\mathrm{b}}^{+}(\mathbf{r}, \mathbf{v}) - S_{\mathrm{b}}^{-}(\mathbf{r}, \mathbf{v}))\delta(\mathbf{r} \in \partial D, \mathbf{v} \cdot \boldsymbol{\nu}(\mathbf{r}) > 0), \tag{41}$$

with $S_{\mathrm{v}}(f_{\mathrm{n,f}}(\mathbf{r}, \mathbf{v}))$ the volumetric source (defined in Eq. (8)), $S_{\mathrm{b}}^{+}(\mathbf{r}, \mathbf{v})$ and $S_{\mathrm{b}}^{-}(\mathbf{r}, \mathbf{v})$ respectively the magnitude of the positive and negative boundary source (defined in Eq. (36)), and $\delta(\mathbf{r} \in \partial D, \mathbf{v} \cdot \boldsymbol{\nu}(\mathbf{r}) > 0)$ the Dirac delta function ($\delta(\mathbf{r} \in \partial D, \mathbf{v} \cdot \boldsymbol{\nu}(\mathbf{r}) > 0) \equiv 0$ if $\mathbf{r} \notin \partial D$ or $\mathbf{v} \cdot \boldsymbol{\nu}(\mathbf{r}) < 0$).

To sample from this source, we use the stratified sampling technique [38, Section 4.3]. This means that the source is priori subdivided in different sub-sources, which are called strata. For the hybrid simulation, we distinguish two strata: a stratum for the positively weighted particles $S_{\mathrm{k}}^{+}(\mathbf{r}, \mathbf{v})$ and a stratum for the negatively weighted particles $S_{\mathrm{k}}^{-}(\mathbf{r}, \mathbf{v})$, given by

$$\begin{aligned} S_{\mathrm{k}}^{+}(\mathbf{r}, \mathbf{v}) &= S_{\mathrm{v}}^{+}(f_{\mathrm{n,f}}(\mathbf{r}, \mathbf{v})) + S_{\mathrm{b}}^{+}(\mathbf{r}, \mathbf{v})\delta(\mathbf{r} \in \partial D, \mathbf{v} \cdot \boldsymbol{\nu}(\mathbf{r}) > 0), & (42) \\ S_{\mathrm{k}}^{-}(\mathbf{r}, \mathbf{v}) &= S_{\mathrm{v}}^{-}(f_{\mathrm{n,f}}(\mathbf{r}, \mathbf{v})) + S_{\mathrm{b}}^{-}(\mathbf{r}, \mathbf{v})\delta(\mathbf{r} \in \partial D, \mathbf{v} \cdot \boldsymbol{\nu}(\mathbf{r}) > 0), & (43) \end{aligned}$$

with $S_{\mathrm{v}}^{+}(f_{\mathrm{n,f}}(\mathbf{r}, \mathbf{v}))$ and $S_{\mathrm{v}}^{-}(f_{\mathrm{n,f}}(\mathbf{r}, \mathbf{v}))$ defined in Section 5.1. The corresponding source strengths (integrals over the velocity space) become

$$\begin{aligned} Q_{\mathrm{k}}^{+}(\mathbf{r}) &= \int_{\mathbf{v}} S_{\mathrm{k}}^{+}(\mathbf{r}, \mathbf{v})\mathrm{d}\mathbf{v} = Q_{\mathrm{v}}^{+}(\mathbf{r}) + Q_{\mathrm{b}}^{+}(\mathbf{r}), & (44) \\ Q_{\mathrm{k}}^{-}(\mathbf{r}) &= \int_{\mathbf{v}} S_{\mathrm{k}}^{-}(\mathbf{r}, \mathbf{v})\mathrm{d}\mathbf{v} = Q_{\mathrm{v}}^{-}(\mathbf{r}) + Q_{\mathrm{b}}^{-}(\mathbf{r}), & (45) \end{aligned}$$

with

$$\begin{aligned} Q_{\mathrm{v}}^{\pm}(\mathbf{r}) &= \int_{\mathbf{v}} S_{\mathrm{v}}^{\pm}(f_{\mathrm{n,f}}(\mathbf{r}, \mathbf{v}))\mathrm{d}\mathbf{v}, & (46) \\ Q_{\mathrm{b}}^{\pm}(\mathbf{r}) &= \int_{\mathbf{v}} S_{\mathrm{b}}^{\pm}(\mathbf{r}, \mathbf{v})\delta(\mathbf{r} \in \partial D, \mathbf{v} \cdot \boldsymbol{\nu}(\mathbf{r}) > 0)\mathrm{d}\mathbf{v}, & (47) \end{aligned}$$

where the superscript + refers to the positive stratum and − to the negative stratum. Due to the linearity of the micro equation, the positive and negative stratum can be treated independently with N^{+} particles for the positive stratum and N^{-} particles for the negative stratum. With a probability $\int_D Q_{\mathrm{v}}^{\pm}(\mathbf{r})\mathrm{d}\mathbf{r} / (\int_D Q_{\mathrm{v}}^{\pm}(\mathbf{r})\mathrm{d}\mathbf{r} + \int_D Q_{\mathrm{b}}^{\pm}(\mathbf{r})\mathrm{d}\mathbf{r})$ (with $\int_D \ldots \mathrm{d}\mathbf{r}$ the volume integral over the domain D) the initial particle position and velocity are sampled from the volumetric source. Otherwise, the particle originates from a boundary source.

We elaborate the sampling procedure for the volumetric source in Section 5.1 and for the boundary source in Section 5.2. In Section 5.3, we explain the recommended

method to simulate the particle trajectories. Finally, the MC estimators for the output quantities of interest, i.e., the kinetic contributions in the macro/fluid equations, are defined in Section 5.4.

5.1. Sampling from volumetric sources

The volumetric source for the micro equation (defined in Eq. (8) with Eq. (2) for $S(f_{\mathrm{n,f}}(\mathbf{r},\mathbf{v}))$) consists of different contributions

$$S_{\mathrm{v}}(f_{\mathrm{n,f}}(\mathbf{r},\mathbf{v})) = S_{\mathrm{r}}(\mathbf{r},\mathbf{v}) - S_{\mathrm{i}}(f_{\mathrm{n,f}}(\mathbf{r},\mathbf{v})) + S_{\mathrm{cx}}(f_{\mathrm{n,f}}(\mathbf{r},\mathbf{v})) + S_{\mathrm{t}}(f_{\mathrm{n,f}}(\mathbf{r},\mathbf{v})), \tag{48}$$

where the different contributions are given by

$$\begin{aligned}
S_{\mathrm{r}}(\mathbf{r},\mathbf{v}) &= \widetilde{f_{\mathrm{i}}}(\mathbf{r},\mathbf{v}) n_{\mathrm{i}}(\mathbf{r}) n_{\mathrm{e}}(\mathbf{r}) K_{\mathrm{r}}(\mathbf{r}), && (49)\\
S_{\mathrm{i}}(f_{\mathrm{n,f}}(\mathbf{r},\mathbf{v})) &= f_{\mathrm{n,f}}(\mathbf{r},\mathbf{v}) n_{\mathrm{e}}(\mathbf{r}) K_{\mathrm{i}}(\mathbf{r}), && (50)\\
S_{\mathrm{cx}}(f_{\mathrm{n,f}}(\mathbf{r},\mathbf{v})) &= (\widetilde{f_{\mathrm{i}}}(\mathbf{r},\mathbf{v}) n_{\mathrm{n}}(\mathbf{r}) - f_{\mathrm{n,f}}(\mathbf{r},\mathbf{v})) n_{\mathrm{i}}(\mathbf{r}) K_{\mathrm{cx}}(\mathbf{r}), && (51)\\
S_{\mathrm{t}}(f_{\mathrm{n,f}}(\mathbf{r},\mathbf{v})) &= -\mathbf{v}\cdot\nabla f_{\mathrm{n,f}}(\mathbf{r},\mathbf{v}). && (52)
\end{aligned}$$

It should be noted that $S_{\mathrm{r}}(\mathbf{r},\mathbf{v}), S_{\mathrm{i}}(f_{\mathrm{n,f}}(\mathbf{r},\mathbf{v})) > 0, \quad \forall \mathbf{r} \in D, \mathbf{v} \in \mathbb{R}^3$, whereas $S_{\mathrm{cx}}(f_{\mathrm{n,f}}(\mathbf{r},\mathbf{v}))$ and $S_{\mathrm{t}}(f_{\mathrm{n,f}}(\mathbf{r},\mathbf{v}))$ can be both positive and negative. Because we assume a perfect drifting Maxwellian for $f_{\mathrm{n,f}}(\mathbf{r},\mathbf{v})$ (see Eq. (34)), the source contribution $S_{\mathrm{t}}(f_{\mathrm{n,f}}(\mathbf{r},\mathbf{v}))$ can be written as

$$S_{\mathrm{t}}(f_{\mathrm{n,f}}(\mathbf{r},\mathbf{v})) = -\widetilde{M}(\mathbf{v};\mathbf{V}_{\mathrm{n}}(\mathbf{r}),T_{\mathrm{n,f}}(\mathbf{r}))\left(\sum_{i=1}^{3} v_i A_{iM}(\mathbf{r}) + \sum_{i=1}^{3}\sum_{j=1}^{3}(v_i v_j A_{iMj}(\mathbf{r}) + v_i v_j^2 A_{iMjj}(\mathbf{r}))\right), \tag{53}$$

with v_i the i-th component of the particle velocity vector defined in an arbitrary orthogonal coordinate system. The coefficients in Eq. (53) are given by

$$\begin{aligned}
A_{iM} &= n_{\mathrm{n}}\left(\left(-\frac{3}{2T_{\mathrm{n,f}}} + \frac{m}{2T_{\mathrm{n,f}}^2}\|\mathbf{V}_{\mathrm{n}}\|^2\right)\nabla_i T_{\mathrm{n,f}} - \frac{m}{T_{\mathrm{n,f}}}\mathbf{V}_{\mathrm{n}}\cdot\nabla_i\mathbf{V}_{\mathrm{n}}\right) + \nabla_i n_{\mathrm{n}}, && (54)\\
A_{iMj} &= n_{\mathrm{n}}\left(-\frac{m}{T_{\mathrm{n,f}}^2}u_{\mathrm{n}j}\nabla_i T_{\mathrm{n,f}} + \frac{m}{T_{\mathrm{n,f}}}\nabla_i u_{\mathrm{n}j}\right), && (55)\\
A_{iMjj} &= n_{\mathrm{n}}\frac{m}{2T_{\mathrm{n,f}}^2}\nabla_i T_{\mathrm{n,f}}, && (56)
\end{aligned}$$

with $u_{\mathrm{n}i}$ and ∇_i the i-th component of respectively the neutral fluid velocity vector and the gradient. We omit the spatial dependence in the notation. Writing $S_{\mathrm{t}}(f_{\mathrm{n,f}}(\mathbf{r},\mathbf{v}))$ as a sum of drifting Maxwellians multiplied by a certain product of the particle velocity components facilitates the particle velocity sampling, see Section 5.1.2.

Now, we define the volumetric sources for the positive and negative stratum in Eqs. (42)-(43) as

$$\begin{aligned}
S_{\mathrm{v}}^{+}(f_{\mathrm{n,f}}(\mathbf{r},\mathbf{v})) &= S_{\mathrm{r}}(\mathbf{r},\mathbf{v}) + S_{\mathrm{cx}}^{+}(f_{\mathrm{n,f}}(\mathbf{r},\mathbf{v})) + S_{\mathrm{t}}^{+}(f_{\mathrm{n,f}}(\mathbf{r},\mathbf{v})), && (57)\\
S_{\mathrm{v}}^{-}(f_{\mathrm{n,f}}(\mathbf{r},\mathbf{v})) &= S_{\mathrm{i}}(\mathbf{r},\mathbf{v}) + S_{\mathrm{cx}}^{-}(f_{\mathrm{n,f}}(\mathbf{r},\mathbf{v})) + S_{\mathrm{t}}^{-}(f_{\mathrm{n,f}}(\mathbf{r},\mathbf{v})), && (58)
\end{aligned}$$

with superscript + for the positive part and superscript - for the negative part of a certain source contribution. To exactly determine these contributions, we define the following operators on a function $f(\mathbf{x})$:

$$[f(\mathbf{x})]_+ \triangleq \begin{cases} f(\mathbf{x}) & \text{if} \quad f(\mathbf{x}) > 0, \\ 0 & \text{else}, \end{cases} \qquad [f(\mathbf{x})]_- \triangleq \begin{cases} -f(\mathbf{x}) & \text{if} \quad f(\mathbf{x}) < 0, \\ 0 & \text{else}. \end{cases} \tag{59}$$

Then, the unknown terms in Eqs. (57)-(58) can be written as

$$S_{\mathrm{cx}}^{+}(f_{\mathrm{n,f}}(\mathbf{r},\mathbf{v})) = [S_{\mathrm{cx}}(f_{\mathrm{n,f}}(\mathbf{r},\mathbf{v}))]_+ , \tag{60}$$

$$S_{\mathrm{cx}}^{-}(f_{\mathrm{n,f}}(\mathbf{r},\mathbf{v})) = [S_{\mathrm{cx}}(f_{\mathrm{n,f}}(\mathbf{r},\mathbf{v}))]_- , \tag{61}$$

$$S_{\mathrm{t}}^{+}(f_{\mathrm{n,f}}(\mathbf{r},\mathbf{v})) = \widetilde{M}(\mathbf{v};\mathbf{V}_{\mathrm{n}}(\mathbf{r}),T_{\mathrm{n,f}}(\mathbf{r}))\left(\sum_{i=1}^{3}[v_i A_{iM}(\mathbf{r})]_- + \sum_{i=1}^{3}\sum_{j=1}^{3}\left(\left[v_i v_j A_{iMj}(\mathbf{r})\right]_- + \left[v_i v_j^2 A_{iMjj}(\mathbf{r})\right]_-\right)\right), \tag{62}$$

$$S_{\mathrm{t}}^{-}(f_{\mathrm{n,f}}(\mathbf{r},\mathbf{v})) = \widetilde{M}(\mathbf{v};\mathbf{V}_{\mathrm{n}}(\mathbf{r}),T_{\mathrm{n,f}}(\mathbf{r}))\left(\sum_{i=1}^{3}[v_i A_{iM}(\mathbf{r})]_+ + \sum_{i=1}^{3}\sum_{j=1}^{3}\left(\left[v_i v_j A_{iMj}(\mathbf{r})\right]_+ + \left[v_i v_j^2 A_{iMjj}(\mathbf{r})\right]_+\right)\right). \tag{63}$$

The corresponding source strengths are

$$Q_{\mathrm{v}}^{+}(\mathbf{r}) = \int_{\mathbf{v}} S_{\mathrm{v}}^{+}(f_{\mathrm{n,f}}(\mathbf{r},\mathbf{v}))\mathrm{d}\mathbf{v} = Q_{\mathrm{r}}(\mathbf{r}) + Q_{\mathrm{cx}}^{+}(\mathbf{r}) + Q_{\mathrm{t}}^{+}(\mathbf{r}), \tag{64}$$

$$Q_{\mathrm{v}}^{-}(\mathbf{r}) = \int_{\mathbf{v}} S_{\mathrm{v}}^{-}(f_{\mathrm{n,f}}(\mathbf{r},\mathbf{v}))\mathrm{d}\mathbf{v} = Q_{\mathrm{i}}(\mathbf{r}) + Q_{\mathrm{cx}}^{-}(\mathbf{r}) + Q_{\mathrm{t}}^{-}(\mathbf{r}), \tag{65}$$

with the different contributions defined as

$$Q_{\mathrm{r}}(\mathbf{r}) = n_{\mathrm{i}}(\mathbf{r})n_{\mathrm{e}}(\mathbf{r})K_{\mathrm{r}}(\mathbf{r}), \tag{66}$$

$$Q_{\mathrm{i}}(\mathbf{r}) = n_{\mathrm{n}}(\mathbf{r})n_{\mathrm{e}}(\mathbf{r})K_{\mathrm{i}}(\mathbf{r}), \tag{67}$$

$$Q_{\mathrm{cx}}^{\pm}(\mathbf{r}) = \int_{\mathbf{v}} S_{\mathrm{cx}}^{\pm}(f_{\mathrm{n,f}}(\mathbf{r},\mathbf{v}))\mathrm{d}\mathbf{v}, \tag{68}$$

$$Q_{\mathrm{t}}^{\pm}(\mathbf{r}) = \int_{\mathbf{v}} S_{\mathrm{t}}^{\pm}(f_{\mathrm{n,f}}(\mathbf{r},\mathbf{v}))\mathrm{d}\mathbf{v}. \tag{69}$$

In Section 5.1.1, we explain the sampling process to determine the initial particle position. Subsequently, the particle velocity is determined, as explained in Section 5.1.2. Then, the particle gets also an initial weight, which is positive for the positive stratum and negative for the negative stratum. Although the particle can be launched now, it happens that the initial position and velocity are rejected and the sampling procedure is repeated. This rejection sampling algorithm is presented in Section 5.1.3.

5.1.1. Initial position

The plasma edge domain is subdivided in N_{D} volumetric grid cells. All variables are discretized in the cell centers. In cell i, the volumetric source is approximated by the midpoint rule:

$$Q_{\mathrm{v},i}^{\pm} = \int_{D_i} Q_{\mathrm{v}}^{\pm}(\mathbf{r})\mathrm{d}\mathbf{r} \approx Q_{\mathrm{v}}^{\pm}(\mathbf{r}_i)\mathcal{V}_i, \tag{70}$$

with $\int_{D_i} \dots \mathrm{d}\mathbf{r}$ the integral over the cell volume, $\mathbf{r}_i$ the coordinate of the cell center and $\mathcal{V}_i$ the cell volume. The + and - sign are used for respectively the positive and negative stratum. This ± shorthand notation is also sometimes used in upcoming sections. The ratio $Q^{\pm}_{\mathrm{v},i} / \sum_{j=1}^{N_\mathrm{D}} Q^{\pm}_{\mathrm{v},j}$ gives the probability that the particle is created in cell i. Then, the initial position is sampled uniformly in the cell volume. The resulting position in cell i is indicated with $\widetilde{\mathbf{r}}$.

5.1.2. Initial velocity and weight

After determining the initial position, we sample from which source contribution the particle originates. With a probability $Q^{\pm}_c(\mathbf{r}_i)\mathcal{V}_i / Q^{\pm}_{\mathrm{v},i}$, the particle originates from contribution c, with c = r for the recombination term, c = i for the ionization term, c = cx for the charge-exchange contribution and c = t for the fluid transport source (see Eqs. (64)-(65) for the definition of the contributions).

Now, we distinguish four different source origins:

1. Recombination (c = r). As can be seen in Eq. (48), the particle velocity needs to be sampled from the ion distribution $\widetilde{f_\mathrm{i}}(\mathbf{r}_i, \mathbf{v})$, which is assumed to be a perfect drifting Maxwellian (see Eq. (4)). Hence, the velocity components in three orthogonal directions have to be sampled each from a normal distribution with average $u_j(\mathbf{r}_i)$ and standard deviation $\sqrt{T_\mathrm{i}(\mathbf{r}_i)/m}$, with index j indicating the direction. The particle gets initial weight $w_0 = 1$.
2. Ionization (c = i). As can be seen in Eq. (48), the particle velocity has to be sampled from the fluid neutral distribution, which we also assume to be a perfect drifting Maxwellian (see Eq. (34)). Hence, the velocity components in three orthogonal directions have to be sampled each from a normal distribution with average $u_{\mathrm{n}j}(\mathbf{r}_i)$ and standard deviation $\sqrt{T_{\mathrm{n,f}}(\mathbf{r}_i)/m}$, with index j indicating the direction. The particle gets initial weight $w_0 = -1$, which is negative because the particle originates from the negative stratum, see Eq. (58).
3. Charge exchange (c = cx). From Eqs. (48), (60)-(61), it can be seen that $\widetilde{f_\mathrm{i}}(\mathbf{r}_i, \mathbf{v}) n_\mathrm{n}(\mathbf{r}_i) n_\mathrm{i}(\mathbf{r}_i) K_\mathrm{cx}(\mathbf{r}_i) \geq S^{+}_\mathrm{cx}(f_{\mathrm{n,f}}(\mathbf{r}_i, \mathbf{v}))$ and $f_{\mathrm{n,f}}(\mathbf{r}_i, \mathbf{v}) n_\mathrm{i}(\mathbf{r}_i) K_\mathrm{cx}(\mathbf{r}_i) \geq S^{-}_\mathrm{cx}(f_{\mathrm{n,f}}(\mathbf{r}_i, \mathbf{v}))$, $\forall \mathbf{v} \in \mathbb{R}^3$. This condition permits the use of the so-called rejection sampling technique [39]. For the positive stratum, we sample the velocity from the ion drifting Maxwellian distribution, whereas we sample from the neutral drifting Maxwellian distribution for the negative stratum. Hence, the sampling distributions in cell i are defined as

$$S^{+}_{\mathrm{cx,s}}(\mathbf{r}_i, \mathbf{v}) = \widetilde{f_\mathrm{i}}(\mathbf{r}_i, \mathbf{v}) n_\mathrm{n}(\mathbf{r}_i) n_\mathrm{i}(\mathbf{r}_i) K_\mathrm{cx}(\mathbf{r}_i), \tag{71}$$

$$S^{-}_{\mathrm{cx,s}}(\mathbf{r}_i, \mathbf{v}) = f_{\mathrm{n,f}}(\mathbf{r}_i, \mathbf{v}) n_\mathrm{i}(\mathbf{r}_i) K_\mathrm{cx}(\mathbf{r}_i). \tag{72}$$

We indicate the resulting sampled velocity with $\widetilde{\mathbf{v}}$. Then, with a probability $S^{\pm}_\mathrm{cx}(\mathbf{r}_i, \widetilde{\mathbf{v}}) / S^{\pm}_{\mathrm{cx,s}}(\mathbf{r}_i, \widetilde{\mathbf{v}})$ the velocity is accepted. Otherwise, the velocity is sampled again from the ion (+) or neutral (-) drifting Maxwellian distribution, until the velocity is accepted. The particle gets initial weight $w_0 = \pm 1$, with the + sign for the positive stratum and the - sign for the negative stratum.
4. Fluid transport (c = t). From Eqs. (62)-(63), it can be seen that the fluid transport source consists of the sum of drifting Maxwellians multiplied by the particle

velocity components to a certain power. To sample from this fluid transport source contribution, we first determine from which term the particle originates. Subsequently, we sample the particle velocity from the corresponding (truncated) Maxwellian multiplied by a certain product of the particle velocity components. Below, we explain this sampling process in more detail.
In general, we can write Eqs. (62)-(63) as

$$S^{\pm}_{\mathrm{t},i}(\mathbf{v}) = \sum_{j=1}^{66} Q^{\pm}_{\mathrm{t},i,j} C_{i,j} \widetilde{M}(\mathbf{v}; \mathbf{V}_{\mathrm{n}}(\mathbf{r}_i), T_{\mathrm{n,f}}(\mathbf{r}_i)) \prod_{k=1}^{3} v_k^{n(j,k)} H(v_k; j, k), \tag{73}$$

with $n(j,k) = 0, \ldots, 3$ a certain power depending on the particular term. The definition of the function $H(v_k; j, k)$ depends on the specific value of j and k. There are three options:

$$H(v_k; j, k) = 1 \quad \forall v_k \in \mathbb{R}, \qquad H(v_k; j, k) = \begin{cases} 0 & \text{if} \quad v_k < 0, \\ 1 & \text{if} \quad v_k \geq 0, \end{cases} \qquad H(v_k; j, k) = \begin{cases} 1 & \text{if} \quad v_k \leq 0, \\ 0 & \text{if} \quad v_k > 0. \end{cases} \tag{74}$$

The first option only occurs when $n(j,k) = 0$. Finally, the constant $C_{i,j}$ guarantees that the velocity distribution is normalized, i.e.,

$$C_{i,j} = \frac{1}{\int_{\mathbf{v}} \widetilde{M}(\mathbf{v}; \mathbf{V}_{\mathrm{n}}(\mathbf{r}_i), T_{\mathrm{n,f}}(\mathbf{r}_i)) \prod_{k=1}^{3} v_k^{n(j,k)} H(v_k; j, k) \mathrm{d}\mathbf{v}}. \tag{75}$$

The ratio $Q^{\pm}_{\mathrm{t},i,j} / \sum_{k=1}^{66} Q^{\pm}_{\mathrm{t},i,k}$ represents the probability that the velocity is sampled from the j-th contribution. The three orthogonal velocity components are sampled independently from the following probability density function:

$$p(v_k; i, j, k) = \frac{v_k^{n(j,k)} N(v_k; u_{\mathrm{n}k}(\mathbf{r}_i), \sqrt{T_{\mathrm{n,f}}(\mathbf{r}_i)/m}) H(v_k; j, k)}{\int_{-\infty}^{\infty} v_k^{n(j,k)} N(v_k; u_{\mathrm{n}k}(\mathbf{r}_i), \sqrt{T_{\mathrm{n,f}}(\mathbf{r}_i)/m}) H(v_k; j, k) \mathrm{d}v_k}, \tag{76}$$

with $N(v; u, \sigma)$ the normal distribution with average u and standard deviation σ. For $n(j,k) = 0$, we have to sample from a complete normal distribution. For $n(j,k) = 1, \ldots, 3$, we have to sample from a truncated normal distribution ($v_k \leq 0$ or $v_k \geq 0$). There are no direct sampling formulas for $n(j,k) = 1, \ldots, 3$. Hence, we use the method of importance sampling [36]. The idea is to sample from an alternative distribution $p^*(v_k; i, j, k)$ and to assign an initial weight to the particle that differs from ± 1, i.e.,

$$w_0 = \pm \frac{\prod_{k=1}^{3} p(v_k; i, j, k)}{\prod_{k=1}^{3} p^*(v_k; i, j, k)}, \tag{77}$$

with + for the positive and − for the negative stratum. Below, we determine an expression for $p^*(v_k; i, j, k)$ and we explain how to sample from this alternative distribution.
Direct sampling from $p(v_k; i, j, k)$, given by Eq. (76), becomes feasible for $n(j,k) = 1, \ldots, 3$ when $u_{\mathrm{n}k}(\mathbf{r}_i) = 0$. Hence, we sample from the alternative distribution

$$p^*(v_k; i, j, k) = \frac{v_k^{n(j,k)} N(v_k; 0, T^*) H(v_k; j, k)}{\int_{-\infty}^{\infty} v_k^{n(j,k)} N(v_k; 0, T^*) H(v_k; j, k) \mathrm{d}v_k}, \tag{78}$$

Table 1: Coefficients $A(n)$ to calculate the alternative temperature with Eq. (79).

	$A(1)$	$A(2)$	$A(3)$
$u_{\mathrm{n}l}(\mathbf{r}_i)v_l < 0$	0.88	0.85	0.84
$u_{\mathrm{n}l}(\mathbf{r}_i)v_l > 0$	0.65	0.57	0.52

with the alternative temperature T^*. The temperature is adapted to obtain an alternative distribution $p^*(v_k; i, j, k)$ that is close to the original distribution $p(v_k; i, j, k)$. This is accomplished by using the following ansatz for T^*:

$$T^* = \frac{T_{\mathrm{n,f}}(\mathbf{r}_i)}{1 \pm A(n(j,k))u_{\mathrm{n}k}(\mathbf{r}_i)/\sqrt{2T_{\mathrm{n,f}}(\mathbf{r}_i)/m}}, \tag{79}$$

with the plus sign in the denominator to sample a negative velocity ($v_k < 0$) and the minus for a positive velocity ($v_k > 0$) and the values for $A(n)$ given in Table 1. This alternative distribution limits the variance of the initial weight in the range $0 \leq |u_{\mathrm{n}k}(\mathbf{r}_i)| \leq \sqrt{2T_{\mathrm{n,f}}(\mathbf{r}_i)/m}$ [31].
The resulting sampled velocity component becomes

$$\widetilde{v}_k = \pm\sqrt{\frac{2T^*}{m}\sum_{l=1}^{n(j,k)+1}\rho_l^2}, \tag{80}$$

with ρ_l a standard normally distributed random number.

The sampled particle velocity is indicated with $\widetilde{\mathbf{v}}$.

5.1.3. Reducing the cancellation error

Now we have sampled the initial particle position, velocity and weight, it is in principle possible to immediately launch the particle. However, this leads to a a large cancellation error. With cancellation error, we mean the fact that the results for the quantities of interest from the MC simulation for the positive and negative stratum become almost equal, but with an opposite sign. This leads to a large statistical error on the net result. In Fig. 2, we illustrate this by plotting the velocity dependence of the volumetric source distribution in a single direction for certain parameter values. E.g., for $v_1 \approx -1 \cdot 10^4$ m/s, the magnitude of both S_{v}^+ and S_{v}^- becomes large. Consequently, there is a large probability to generate a particle with a velocity component around this value. However, the positive and negative contributions will more or less cancel each other in the overall result.

To overcome this issue, we elaborate a method to sample from $[S_{\mathrm{v}}(\mathbf{r}, \mathbf{v})]_+$ for the positive stratum and $[S_{\mathrm{v}}(\mathbf{r}, \mathbf{v})]_-$ for the negative stratum (with the square bracket operators defined in Eq. (59)). Then, we sample immediately from the blue solid curve in Fig. 2. Due to the complexity of $[S_{\mathrm{v}}(\mathbf{r}, \mathbf{v})]_\pm$, we do not sample directly from this distribution, but we use the rejection sampling technique. We sample the position and velocity as explained in Sections 5.1.1-5.1.2. This results in the position $\widetilde{\mathbf{r}}$ and velocity $\widetilde{\mathbf{v}}$. Subsequently, we calculate

$$\eta^\pm = [S_{\mathrm{v}}(\widetilde{\mathbf{r}}, \widetilde{\mathbf{v}})]_\pm / S_{\mathrm{v}}^\pm(\widetilde{\mathbf{r}}, \widetilde{\mathbf{v}}). \tag{81}$$

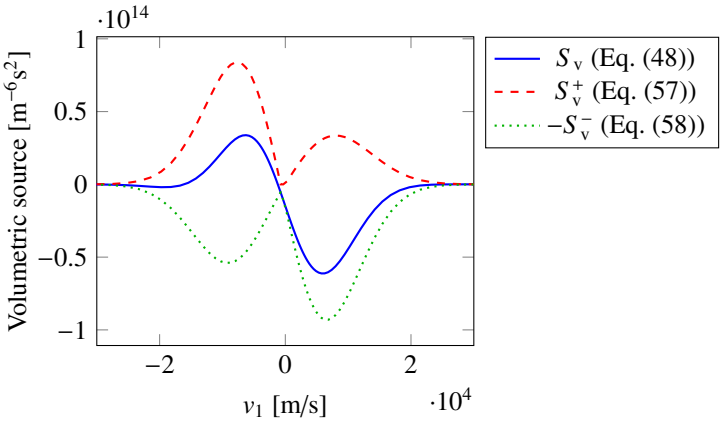

Figure 2: Volumetric source distribution at a fixed location as a function of the single velocity component v_1 for $v_2 = v_3 = 0$. The chosen parameter values are $K_\mathrm{r} = K_\mathrm{i} = 0$, $K_\mathrm{cx} = 10^{-14}$ m^3/s, $n_\mathrm{i} = n_\mathrm{e} = n_\mathrm{n} = 10^{21}$ m^{-3}, $u_1 = 1\,000$ m/s, $u_{\mathrm{n}1} = 500$ m/s, $u_2 = u_3 = u_{\mathrm{n}2} = u_{\mathrm{n}3} = 0$, $T_\mathrm{i} = T_\mathrm{e} = T_{\mathrm{n,f}} = 1$ eV, $\nabla_1 n_\mathrm{n} = 6 \cdot 10^{22}$ m^{-4}, $\nabla_1 u_{\mathrm{n}1} = 10^5$ s^{-1} and $\nabla_1 T_{\mathrm{n,f}} = 15$ eV/m. All gradients in the second and third direction are zero.

The value of $\eta^\pm$ gives the probability that the sampled position and velocity are accepted and the particle is launched. Otherwise, we sample again from $S_\mathrm{k}^\pm(\mathbf{r}, \mathbf{v})$, as defined in Eqs. (42)-(43). Note that it is possible that the particle now originates from a boundary source (Section 5.2).

It should be noted that also different expressions can be used for $S_\mathrm{v}^\pm(\mathbf{r}, \mathbf{v})$ instead of Eqs. (57)-(58), as long as $S_\mathrm{v}^+(\mathbf{r}, \mathbf{v}) \geq [S_\mathrm{v}(\mathbf{r}, \mathbf{v})]_+$ and $S_\mathrm{v}^-(\mathbf{r}, \mathbf{v}) \geq [S_\mathrm{v}(\mathbf{r}, \mathbf{v})]_- \; \forall \mathbf{r} \in D, \; \mathbf{v} \in \mathbb{R}^3$. However, the expressions given in this paper lead to a relatively large acceptance rate and hence, a low computational cost for the sampling process.

Finally, also the total volumetric source strength $Q_{\mathrm{v,tot}}^\pm = \int_D \int_\mathbf{v} [S_\mathrm{v}(\mathbf{r}, \mathbf{v})]_\pm \, \mathrm{d}\mathbf{r}\mathrm{d}\mathbf{v}$ is estimated as

$$\widehat{Q}_{\mathrm{v,tot}}^\pm = < \eta^\pm > \sum_{i=1}^{N_\mathrm{D}} Q_{\mathrm{v},i}^\pm, \tag{82}$$

with $< \eta^\pm >$ the average value of $\eta^\pm$ for all rejection iterations for all particles and $Q_{\mathrm{v},i}^\pm$ given in Eq. (70). The hat on top of a variable means that it corresponds to an MC estimate. This total volumetric source strength estimate is needed in Section 5.4 to scale the MC tallies.

5.2. Sampling from boundary sources

For the positive and negative boundary stratum we have respectively the boundary source distribution $S_\mathrm{b}^+(\mathbf{r}_\mathrm{b}, \mathbf{v})$ and $S_\mathrm{b}^-(\mathbf{r}_\mathrm{b}, \mathbf{v})$ with $\mathbf{r}_\mathrm{b} \in \partial D$ and $\mathbf{v} \cdot \boldsymbol{\nu}(\mathbf{r}_\mathrm{b}) > 0$, defined in Eq. (36). If the numerical grid consists of N_b boundary faces, the corresponding source strengths at face j are approximated by the midpoint rule. The source strength of the positive boundary stratum becomes

$$Q_{\mathrm{b},j}^+ = \int_{\mathbf{v}\cdot\boldsymbol{\nu}(\mathbf{r}_{\mathrm{b},j})>0} S_\mathrm{b}^+(\mathbf{r}_{\mathrm{b},j}, \mathbf{v}) \mathrm{d}\mathbf{v} \mathcal{A}_j = Q_{\mathrm{b,rec},j}^+ + Q_{\mathrm{b,refl},j}^+, \tag{83}$$

with

$$Q^{+}_{\mathrm{b,rec},j} = -R^{\mathrm{i}}(\mathbf{r}_{\mathrm{b},j})\mathbf{V}_{\mathrm{i}}(\mathbf{r}_{\mathrm{b},j})\cdot\boldsymbol{\nu}(\mathbf{r}_{\mathrm{b},j})\mathcal{A}_j, \quad Q^{+}_{\mathrm{b,refl},j} = -R^{\mathrm{n}}(\mathbf{r}_{\mathrm{b},j}) \int_{\mathbf{v}'\cdot\boldsymbol{\nu}(\mathbf{r}_{\mathrm{b},j})<0} f_{\mathrm{n,f}}(\mathbf{r}_{\mathrm{b},j},\mathbf{v}')(\mathbf{v}'\cdot\boldsymbol{\nu}(\mathbf{r}_{\mathrm{b},j}))\mathrm{d}\mathbf{v}'\mathcal{A}_j, \tag{84}$$

with $\mathbf{r}_{\mathrm{b},j}$ the coordinate of the center of face j and $\mathcal{A}_j$ the face area. For the negative boundary stratum, the source strength becomes

$$Q^{-}_{\mathrm{b},j} = \int_{\mathbf{v}\cdot\boldsymbol{\nu}(\mathbf{r}_{\mathrm{b},j})>0} S^{-}_{\mathrm{b}}(\mathbf{r}_{\mathrm{b},j},\mathbf{v})\mathrm{d}\mathbf{v}\mathcal{A}_j = \int_{\mathbf{v}\cdot\boldsymbol{\nu}(\mathbf{r}_{\mathrm{b},j})>0} f_{\mathrm{n,f}}(\mathbf{r}_{\mathrm{b},j},\mathbf{v})(\mathbf{v}\cdot\boldsymbol{\nu}(\mathbf{r}_{\mathrm{b},j}))\mathrm{d}\mathbf{v}\mathcal{A}_j, \tag{85}$$

The integrals in Eqs. (84)-(85) can be calculated analytically for a perfect drifting Maxwellian for $f_{\mathrm{n,f}}(\mathbf{r},\mathbf{v})$ (see Eq. (34)). The ratio $Q^{\pm}_{\mathrm{b},j}/\sum_{k=1}^{N_{\mathrm{b}}} Q^{\pm}_{\mathrm{b},k}$ gives the probability that the particle is born at face j. Then, the initial position is uniformly sampled at the face.

Because of the Maxwellian ion and neutral distributions, the initial particle velocity has to be sampled from a truncated Maxwellian. In Section 5.2.1, we consider the positive stratum. The negative stratum is discussed in Section 5.2.2.

5.2.1. Positive stratum

For the positive stratum, with a probability $Q^{+}_{\mathrm{b,rec},j}/Q^{+}_{\mathrm{b},j}$, with $Q^{+}_{\mathrm{b,rec},j}$ and $Q^{+}_{\mathrm{b},j}$ defined in Eq. (83), the particle originates from the recycling source, which is already present in a full kinetic simulation. In this case, the particle velocity is sampled at the sheath entrance. The probability density function for the normal velocity component $v_{\mathrm{se},1}$ for the recycling source is given by

$$p^{+}_{\mathrm{rec}}(v_{\mathrm{se},1}) = \frac{v_{\mathrm{se},1}N(v_{\mathrm{se},1};u_1(\mathbf{r}_{\mathrm{b},j}),\sqrt{T_{\mathrm{i}}(\mathbf{r}_{\mathrm{b},j})/m})}{\int_{-\infty}^{0} v_{\mathrm{se},1}N(v_{\mathrm{se},1};u_1(\mathbf{r}_{\mathrm{b},j}),\sqrt{T_{\mathrm{i}}(\mathbf{r}_{\mathrm{b},j})/m})\mathrm{d}v_{\mathrm{se},1}}, \quad \text{with} \quad v_{\mathrm{se},1} \leq 0. \tag{86}$$

The negative value of $v_{\mathrm{se},1}$ means that the particle is flying towards the boundary surface. Eq. (86) is similar as Eq. (76) for the power $n = 1$, but with ion macroscopic properties instead of the neutral properties. Hence, we re-use the non-analog sampling procedure from Section 5.1.2. The tangential velocity components $v_{\mathrm{se},2}$ and $v_{\mathrm{se},3}$ are sampled from complete normal distributions with the ion properties. Next, the particle is accelerated in the normal direction by the sheath potential. This leads to the particle velocity $\mathbf{v} = \begin{bmatrix} v_1 & v_2 & v_3 \end{bmatrix}^T$. The tangential components remain unchanged, i.e., $v_2 = v_{\mathrm{se},2}$ and $v_3 = v_{\mathrm{se},3}$. The normal component becomes

$$v_1 = -\sqrt{v^2_{\mathrm{se},1} + \frac{2}{m}\delta^{\mathrm{pot}}_{\mathrm{sh}}T_{\mathrm{e}}}, \tag{87}$$

with $\delta^{\mathrm{pot}}_{\mathrm{sh}}$ the sheath transmission coefficient.

For the reflected part ($Q^{+}_{\mathrm{b,refl},j}$ in Eq. (83)), the normal velocity component probability density function becomes

$$p^{+}_{\mathrm{refl}}(v_1) = \frac{v_1 N(v_1;u_{\mathrm{n1}}(\mathbf{r}_{\mathrm{b},j}),\sqrt{T_{\mathrm{n,f}}(\mathbf{r}_{\mathrm{b},j})/m})}{\int_{-\infty}^{0} v_1 N(v_1;u_{\mathrm{n1}}(\mathbf{r}_{\mathrm{b},j}),\sqrt{T_{\mathrm{n,f}}(\mathbf{r}_{\mathrm{b},j})/m})\mathrm{d}v_1}, \quad \text{with} \quad v_1 \leq 0, \tag{88}$$

which is similar as Eq. (86), but with neutral bulk velocity and (fluid) temperature. Again, the tangential velocity components are sampled from full normal distributions. The resulting particle velocity for the positive stratum is oriented towards the boundary surface. This implies that the reflection kernel is immediately applied, as explained in Section 5.3.

5.2.2. Negative stratum

For the negative stratum, there is only a single contribution. Its normal velocity component probability density function is given by

$$p^{-}(v_1) = \frac{v_1 N(v_1; u_{\mathrm{n}1}(\mathbf{r}_{\mathrm{b},j}),\ \sqrt{T_{\mathrm{n,f}}(\mathbf{r}_{\mathrm{b},j})/m})}{\int_0^\infty v_1 N(v_1; u_{\mathrm{n}1}(\mathbf{r}_{\mathrm{b},j}),\ \sqrt{T_{\mathrm{n,f}}(\mathbf{r}_{\mathrm{b},j})/m})\mathrm{d}v_1}, \quad \text{with} \quad v_1 \geq 0. \tag{89}$$

Again, the non-analog sampling procedure from Section 5.1.2 is used with full normal distributions (with fluid neutral properties) for the tangential velocity components. Because $v_1 \geq 0$, the particle is immediately sent into the plasma region without reflection.

5.3. Simulating the particle trajectories

At this point, we have determined the initial particle position, velocity and weight. In contrast to the MC simulation of the full kinetic equation (Eq. (1)), there are no (volumetric) scattering charge-exchange collisions for the hybrid micro equation (Eq. (8)). Volumetrically, there only remains absorption with rate $R_{\mathrm{t}}(\mathbf{r})$, defined in Eq. (3). Whereas the charge-exchange collision kernel is the stiff term in the full kinetic equation in terms that it leads to very short times between two collision events, the charge-exchange events are now mostly contained in the fluid part for the micro-macro model. This means that the stiffness of the collision operator disappears in the micro-macro model with this specific type of MC simulation. However, it should be noted that also the micro-macro model might suffer from the stiffness of the collision operator for time-dependent simulations, see, e.g., Ref. [20]. Time-dependent simulations are out of the scope of this paper.

If we use the analog simulation strategy, which is the default simulation type in the EIRENE code [31], as explained in the beginning of Section 5, the particle is rapidly absorbed during the hybrid simulation due to the lack of scattering events. This leads to very short particle trajectories. According to Ref. [37], it is not recommended to use an analog simulation for absorption-dominated cases.

Instead of an analog simulation, we use a non-analog track-length type simulation for the micro equation, where volumetric absorption is taken into account during the particle trajectory. After crossing cell i, the particle weight is lowered to $w \exp(-R_{\mathrm{t}}(\mathbf{r}_i) d_i / \|\widetilde{\mathbf{v}}\|)$, with w the weight before entering cell i, d_i the traveled distance in cell i and $\widetilde{\mathbf{v}}$ the particle velocity. From the moment the magnitude of the weight has reached a user-imposed minimum value, the particle trajectory is ended.

When the particle hits a boundary surface, the reflection kernel is applied. In our case, we use the TRIM code database similar as in the EIRENE code. More details about the use of the TRIM database can be found in the EIRENE manual [31]. After reflection at position $\mathbf{r}_{\mathrm{b}}$, the particle weight is multiplied by $R^{\mathrm{n}}(\mathbf{r}_{\mathrm{b}})$ to take into account the absorbed fraction.

Finally, it should be noted that the reflection kernel is also applied to the boundary source of the positive stratum ($S_{\mathrm{b}}^{+}(\mathbf{r}_{\mathrm{b}}, \mathbf{v})$), as already mentioned in Section 5.2.1. However, for this source, the weight is not multiplied by $R^{\mathrm{n}}(\mathbf{r}_{\mathrm{b}})$ after reflection, because the recycling and reflection coefficients, respectively $R^{\mathrm{i}}(\mathbf{r}_{\mathrm{b}})$ and $R^{\mathrm{n}}(\mathbf{r}_{\mathrm{b}})$, are already accounted for in the source strengths (see Eq. (83)).

5.4. Estimating the tallies

Now, we are able to generate the particle trajectories from place of birth until death. In this section, we elaborate the estimators for the kinetic quantities of interest that appear in the macro/fluid equations, which are the kinetic pressure $p_{\mathrm{n,k}}$, stress tensor $\Pi_{\mathrm{n,k}}$, heat flux vector $\mathbf{q}_{\mathrm{n,k}}$ and boundary flux densities $\mathbf{\Gamma}^{\mathrm{n}}_{\mu,\mathrm{k}}$.

According to Ref. [37], a track-length estimator in combination with a non-analog track-length type simulation performs well with respect to the variance for a certain computational time for absorption-dominated cases. Then, the estimate for a certain macroscopic property Φ in cell i becomes

$$\begin{aligned}
\widehat{\Phi}_i^{\pm} &= \frac{1}{N^{\pm}} \frac{\widehat{Q}_{\mathrm{t}}^{\pm}}{\mathcal{V}_i} \sum_{k=1}^{N_i^{\pm}} \mu(\mathbf{v}_k^{\pm}) \frac{1}{\|\mathbf{v}_k^{\pm}\|} \int_0^{d_k^{\pm}} w_k^{\pm}(s) \mathrm{d}s \\
&= \frac{1}{N^{\pm}} \frac{\widehat{Q}_{\mathrm{t}}^{\pm}}{\mathcal{V}_i} \sum_{k=1}^{N_i^{\pm}} \mu(\mathbf{v}_k^{\pm}) \underbrace{\frac{w_{k,0}^{\pm}}{R_{\mathrm{t}}(\mathbf{r}_i)} \left(1 - \exp\left(-R_{\mathrm{t}}(\mathbf{r}_i) \frac{d_k^{\pm}}{\|\mathbf{v}_k^{\pm}\|}\right)\right)}_{w_k^{\pm}},
\end{aligned} \tag{90}$$

with k the particle index, superscript + for the positive stratum and - for the negative stratum, $N_i^{\pm}$ the total number of particle trajectories through cell i and $d_k^{\pm}$ the distance the particle with velocity $\mathbf{v}_k^{\pm}$ and weight $w_k^{\pm}$ travels in the particular cell. Note that the weight remains always positive for the positive stratum ($w_k^{+} \geq 0$) and negative for the negative stratum ($w_k^{-} \leq 0$). The weight of the particle when it enters the cell is $w_{k,0}^{\pm}$. The moment corresponding to the tally is indicated with $\mu(\mathbf{v})$. The tally is scaled with the total source estimate $\widehat{Q}_{\mathrm{t}}^{\pm}$ that follows from

$$\widehat{Q}_{\mathrm{t}}^{\pm} = \widehat{Q}_{\mathrm{v,tot}}^{\pm} + \sum_{j=1}^{N_{\mathrm{b}}} Q_{\mathrm{b},j}^{\pm}, \tag{91}$$

with the expression for $\widehat{Q}_{\mathrm{v,tot}}^{\pm}$ in Eq. (82). For upcoming expressions we use the notation $w_k^{\pm}$ as a shorthand notation, as indicated in Eq. (90). The total tally from the combined positive and negative stratum becomes

$$\widehat{\Phi}_i = \widehat{\Phi}_i^{+} + \widehat{\Phi}_i^{-}. \tag{92}$$

The estimates of the total second order moment $\mathcal{M}_{\mathrm{k},i}$ and heat flux vector $\mathbf{q}_{\mathrm{n,k},i}$ in cell i become

$$\left[\widehat{\mathcal{M}}_{\mathrm{k},i}^{\pm} \quad \widehat{\mathbf{q}}_{\mathrm{n,k},i}^{\pm}\right] = \frac{1}{N^{\pm}} \frac{\widehat{Q}_{\mathrm{t}}^{\pm}}{\mathcal{V}_i} \sum_{k=1}^{N_i^{\pm}} m \left[\mathbf{v}_k^{\pm}\mathbf{v}_k^{\pm} \quad \tfrac{1}{2}\|\mathbf{v}_k^{\pm}\|^2 \mathbf{v}_k^{\pm}\right] w_k^{\pm}. \tag{93}$$

Then, the kinetic pressure and stress tensor tallies follow from

$$\widehat{p}^{\pm}_{\mathrm{n,k},i} = \frac{1}{3}\mathrm{trace}\left(\widehat{\mathcal{M}}^{\pm}_{\mathrm{k},i}\right), \qquad \widehat{\Pi}^{\pm}_{\mathrm{n,k},i} = \widehat{\mathcal{M}}^{\pm}_{\mathrm{k},i} - \widehat{p}^{\pm}_{\mathrm{n,k},i}\mathbb{I}. \tag{94}$$

For estimating the kinetic boundary flux density $\mathbf{\Gamma}^{\mathrm{n}}_{\mu,\mathrm{k},j}$ at face j, the particles score at a boundary surface instead of in a volumetric cell. Hence, we use a collision estimator:

$$\widehat{\mathbf{\Gamma}}^{\pm}_{\mu,\mathrm{k},j} = \frac{1}{N^{\pm}}\frac{\widehat{Q}^{\pm}_{\mathrm{t}}}{\mathcal{A}_j}\sum_{k=1}^{N^{\pm}_j}\boldsymbol{\mu}(\mathbf{v}^{\pm}_k)\underbrace{w^{\pm}_k\frac{\mathbf{v}^{\pm}_k\cdot\boldsymbol{\nu}(\mathbf{r}_{\mathrm{b},j})}{\|\mathbf{v}^{\pm}_k\cdot\boldsymbol{\nu}(\mathbf{r}_{\mathrm{b},j})\|}}_{w^{\pm}_{k,\mathrm{b}}}, \tag{95}$$

with $N^{\pm}_j$ the total number of times the particles hit and leave the boundary face and the moment vector $\boldsymbol{\mu}(\mathbf{v})$ defined in Eq. (11). Again, we introduce a shorthand notation $(w^{\pm}_{k,\mathrm{b}})$.

6. Solution procedure for the coupled fluid-kinetic equations

The fluid equations are discretized on a staggered grid by means of finite volumes with a first-order upwind scheme. With staggered grid, we mean that the scalar quantities are discretized in the cell centers, whereas the vector quantities are discretized at the cell faces. For the MC part, we need the fluid properties in the cell centers. Hence, we use linear interpolation to obtain the staggered variables in the cell centers. For the fluid equations, we use a sequential solver with a false-time-stepping procedure with time step Δt and implicit Euler time integration. In addition, under-relaxation is used with a factor α. The restrictions for Δt and α follow from the stability conditions for the macro model discretization. In Section 7.1, we give the time-step and relaxation values for the different simulations.

In every iteration, we solve a linearized correction equation for every (fluid) state equation for the correction vector $\Delta\Phi^n$, with n the iteration number. In cell i, this finite-volume discretized correction equation can be written as

$$\frac{\Delta\Phi^n_i}{\Delta t}\mathcal{V}_i = R_i(\Phi^{n-1}) + \frac{\partial R_i}{\partial\Phi}(\Phi^{n-1})\Delta\Phi^n, \tag{96}$$

with Φ^n the vector of the particular state variable in the different cells for iteration n, R_i the residual of the discretized equation and $\Delta\Phi^n_i$ the correction in cell i. The updated state becomes $\Phi^n = \Phi^{n-1} + \alpha\Delta\Phi^n$.

The micro and macro equations are solved in an iterative way. We start from a certain initial guess for the fluid and kinetic properties, e.g., the solution of the pure fluid model without kinetic corrections. Then, an MC simulation of the micro part is performed. Subsequently, the fluid state is updated using the obtained kinetic contributions. This process is repeated until the residuals of the fluid equations are statistically fluctuating around a constant value. This indicates the end of the transient phase. From that moment, we keep iterating and start averaging the output variables of interest. This random noise averaging technique from Ref. [7] is an excellent method to eliminate the noise from the final results.

After a single MC simulation of the micro part, conditions (7) and (13) to guarantee that the kinetic neutrals contain no net mass and particle flux are violated. Additionally, for the model with energy equation (model 3), also condition (33), which imposes zero kinetic pressure, is violated. In Ref. [20], the authors recommend to add a projection step to guarantee that all conditions for this specific hybrid approach are fulfilled. This projection step was not yet included in the hybrid simulations of Ref. [28], but is added in this paper. The projection step alters the particle weights $w_k^{\pm}$, defined in Eq. (90) as the weight of an entering particle multiplied by the weight reduction factor due to absorption events, to $\widetilde{w}_k^{\pm}$ by solving following least-squares optimization problem:

$$\min_{\widetilde{w}_k^+, \widetilde{w}_k^-} \frac{1}{2} \left(\sum_{k=1}^{N_i^+} (\widetilde{w}_k^+ - w_k^+)^2 + \sum_{k=1}^{N_i^-} (\widetilde{w}_k^- - w_k^-)^2 \right) \quad \text{s.t.} \quad \frac{1}{N^+} \frac{\widehat{Q}_\mathrm{t}^+}{\mathcal{V}_i} \sum_{k=1}^{N_i^+} \boldsymbol{\mu}_\mathrm{f}(\mathbf{v}_k^+) \widetilde{w}_k^+ + \frac{1}{N^-} \frac{\widehat{Q}_\mathrm{t}^-}{\mathcal{V}_i} \sum_{k=1}^{N_i^-} \boldsymbol{\mu}_\mathrm{f}(\mathbf{v}_k^-) \widetilde{w}_k^- = 0, \tag{97}$$

with $\boldsymbol{\mu}_\mathrm{f}(\mathbf{v}) = \begin{bmatrix} 1 & \mathbf{v}^T \end{bmatrix}^T$ for the fluid models without neutral energy equation (models 1-2) and $\boldsymbol{\mu}_\mathrm{f}(\mathbf{v}) = \begin{bmatrix} 1 & \mathbf{v}^T & \|\mathbf{v}\|^2 \end{bmatrix}^T$ for the model with energy equation (model 3). Whereas the macro equations were already discretized in a conservative way by means of finite volumes, the hard constraints in Eq. (97) now also guarantee conservation of mass, momentum and energy of the coupled micro-macro system, at the expense of a bias introduced by adapting the particle weights. With the objective function of Eq. (97), we try to minimize the bias. The optimization problem of Eq. (97) has to be solved for every grid cell in the interior of the domain, i.e., $i = 1, \ldots, N_\mathrm{D}$. The solution of this optimization problem gives

$$\widetilde{w}_k^{\pm} = w_k^{\pm} - \boldsymbol{\lambda}^T \frac{1}{N^{\pm}} \frac{\widehat{Q}_\mathrm{t}^{\pm}}{\mathcal{V}_i} \boldsymbol{\mu}_\mathrm{f}(\mathbf{v}_k^{\pm}), \tag{98}$$

with the vector of Lagrange multipliers $\boldsymbol{\lambda}$ as the solution of

$$A_\lambda \boldsymbol{\lambda} = \frac{1}{N^+} \frac{\widehat{Q}_\mathrm{t}^+}{\mathcal{V}_i} \sum_{k=1}^{N_i^+} \boldsymbol{\mu}_\mathrm{f}(\mathbf{v}_k^+) w_k^+ + \frac{1}{N^-} \frac{\widehat{Q}_\mathrm{t}^-}{\mathcal{V}_i} \sum_{k=1}^{N_i^-} \boldsymbol{\mu}_\mathrm{f}(\mathbf{v}_k^-) w_k^-, \tag{99}$$

with the matrix A_λ given by

$$A_\lambda = \left(\frac{1}{N^+} \frac{\widehat{Q}_\mathrm{t}^+}{\mathcal{V}_i} \right)^2 \sum_{k=1}^{N_i^+} \boldsymbol{\mu}_\mathrm{f}(\mathbf{v}_k^+) \boldsymbol{\mu}_\mathrm{f}^T(\mathbf{v}_k^+) + \left(\frac{1}{N^-} \frac{\widehat{Q}_\mathrm{t}^-}{\mathcal{V}_i} \right)^2 \sum_{k=1}^{N_i^-} \boldsymbol{\mu}_\mathrm{f}(\mathbf{v}_k^-) \boldsymbol{\mu}_\mathrm{f}^T(\mathbf{v}_k^-). \tag{100}$$

The elements of A_λ can easily be calculated during the MC simulation.

It is not required to save all particle weights. The adapted tally in cell i after the projection step for a particular moment $\mu(\mathbf{v})$ becomes

$$\widetilde{\Phi}_i^{\pm} = \frac{1}{N^{\pm}} \frac{\widehat{Q}_\mathrm{t}^{\pm}}{\mathcal{V}_i} \sum_{k=1}^{N_i^{\pm}} \mu(\mathbf{v}_k^{\pm}) \widetilde{w}_k^{\pm} = \underbrace{\frac{1}{N^{\pm}} \frac{\widehat{Q}_\mathrm{t}^{\pm}}{\mathcal{V}_i} \sum_{k=1}^{N_i^{\pm}} \mu(\mathbf{v}_k^{\pm}) w_k^{\pm}}_{\widehat{\Phi}_i^{\pm}} - \boldsymbol{\lambda}^T \underbrace{\left(\frac{1}{N^{\pm}} \frac{\widehat{Q}_\mathrm{t}^{\pm}}{\mathcal{V}_i} \right)^2 \sum_{k=1}^{N_i^{\pm}} \mu(\mathbf{v}_k^{\pm}) \boldsymbol{\mu}_\mathrm{f}(\mathbf{v}_k^{\pm})}_{\widetilde{\boldsymbol{\mu}}_i^{\pm}}, \tag{101}$$

where $\widehat{\Phi}_i^{\pm}$ corresponds to the MC estimate before the projection step and $\widetilde{\boldsymbol{\mu}}_i^{\pm}$ has additionally to be calculated during the micro simulation.

The process is repeated for the boundary cells, for which the least-squares optimization problem becomes

$$\min_{\widetilde{w}_{k,\mathrm{b}}^{+},\widetilde{w}_{k,\mathrm{b}}^{-}} \frac{1}{2}\left(\sum_{k=1}^{N_j^+}(\widetilde{w}_{k,\mathrm{b}}^{+}-w_{k,\mathrm{b}}^{+})^2+\sum_{k=1}^{N_j^-}(\widetilde{w}_{k,\mathrm{b}}^{-}-w_{k,\mathrm{b}}^{-})^2\right)$$

$$\text{s.t.}\quad \frac{1}{N^+}\frac{\widehat{Q}_{\mathrm{t}}^{+}}{\mathcal{A}_j}\sum_{k=1}^{N_j^+}\boldsymbol{\mu}_{\mathrm{f}}(\mathbf{v}_k^{+})\frac{\widetilde{w}_{k,\mathrm{b}}^{+}}{\mathbf{v}_k^{+}\cdot\boldsymbol{\nu}(\mathbf{r}_{\mathrm{b},j})}+\frac{1}{N^-}\frac{\widehat{Q}_{\mathrm{t}}^{-}}{\mathcal{A}_j}\sum_{k=1}^{N_j^-}\boldsymbol{\mu}_{\mathrm{f}}(\mathbf{v}_k^{-})\frac{\widetilde{w}_{k,\mathrm{b}}^{-}}{\mathbf{v}_k^{-}\cdot\boldsymbol{\nu}(\mathbf{r}_{\mathrm{b},j})}=0, \quad (102)$$

for all boundary faces $j = 1,\dots,N_{\mathrm{b}}$ and $w_{k,\mathrm{b}}^{\pm}$ defined in Eq. (95). The adapted weights become

$$\widetilde{w}_{k,\mathrm{b}}^{\pm}=w_{k,\mathrm{b}}^{\pm}-\boldsymbol{\lambda}^T\frac{1}{N^{\pm}}\frac{\widehat{Q}_{\mathrm{t}}^{\pm}}{\mathcal{A}_j}\frac{1}{\mathbf{v}_k^{\pm}\cdot\boldsymbol{\nu}(\mathbf{r}_{\mathrm{b},j})}\boldsymbol{\mu}_{\mathrm{f}}(\mathbf{v}_k^{\pm}), \quad (103)$$

with $\boldsymbol{\lambda}$ the solution of

$$\left(\left(\frac{1}{N^+}\frac{\widehat{Q}_{\mathrm{t}}^{+}}{\mathcal{A}_j}\right)^2\sum_{k=1}^{N_j^+}\frac{1}{(\mathbf{v}_k^{+}\cdot\boldsymbol{\nu}(\mathbf{r}_{\mathrm{b},j}))^2}\boldsymbol{\mu}_{\mathrm{f}}(\mathbf{v}_k^{+})\boldsymbol{\mu}_{\mathrm{f}}^T(\mathbf{v}_k^{+})+\left(\frac{1}{N^-}\frac{\widehat{Q}_{\mathrm{t}}^{-}}{\mathcal{A}_j}\right)^2\sum_{k=1}^{N_j^-}\frac{1}{(\mathbf{v}_k^{-}\cdot\boldsymbol{\nu}(\mathbf{r}_{\mathrm{b},j}))^2}\boldsymbol{\mu}_{\mathrm{f}}(\mathbf{v}_k^{-})\boldsymbol{\mu}_{\mathrm{f}}^T(\mathbf{v}_k^{-})\right)\boldsymbol{\lambda}$$

$$=\sum_{k=1}^{N_j^+}\frac{1}{\mathbf{v}_k^{+}\cdot\boldsymbol{\nu}(\mathbf{r}_{\mathrm{b},j})}\boldsymbol{\mu}_{\mathrm{f}}(\mathbf{v}_k^{+})w_{k,\mathrm{b}}^{+}+\sum_{k=1}^{N_j^-}\frac{1}{\mathbf{v}_k^{-}\cdot\boldsymbol{\nu}(\mathbf{r}_{\mathrm{b},j})}\boldsymbol{\mu}_{\mathrm{f}}(\mathbf{v}_k^{-})w_{k,\mathrm{b}}^{-}. \quad (104)$$

Then, the adapted kinetic boundary flux density for a certain moment $\mu(\mathbf{v}_k)$ becomes

$$\widetilde{\Gamma}_{\mu,\mathrm{k},j}^{\mathrm{n}\pm}=\widehat{\Gamma}_{\mu,\mathrm{k},j}^{\mathrm{n}\pm}-\boldsymbol{\lambda}^T\left(\frac{1}{N^{\pm}}\frac{\widehat{Q}_{\mathrm{t}}^{\pm}}{\mathcal{A}_j}\right)^2\sum_{k=1}^{N_j^{\pm}}\frac{\mu(\mathbf{v}_k^{\pm})}{\mathbf{v}_k^{\pm}\cdot\boldsymbol{\nu}(\mathbf{r}_{\mathrm{b},j})}\boldsymbol{\mu}_{\mathrm{f}}(\mathbf{v}_k^{\pm}). \quad (105)$$

In this paper, we do not solve the plasma equations. However, the numerical grid is magnetic-field aligned and also typical for the disretization of the plasma equations. This grid choice limits the numerical diffusion due to the plasma anisotropy. Hence, the grid can be retained for future coupled fluid plasma – hybrid neutral simulations. As future research, it might be recommended to explore a different discretization for the plasma and neutral equations to increase the performance w.r.t. accuracy and computational time.

7. Results

In this section, we illustrate the performance of the method. In Section 7.1, we describe the test case. In Section 7.2, we evaluate the global balances for the solved fluid moments during the iterative process and show that the models are conservative. Next, we compare the resulting plasma sources for the full kinetic, full fluid (without kinetic corrections) and hybrid simulations in Section 7.3. Finally, we assess the performance of the hybrid approach by evaluating the reduction of the computational time compared to an MC simulation of the full kinetic equation for the same statistical error on a certain source in Section 7.4.

7.1. Description of the test case

The test case is similar to the case from Ref. [28], i.e., a single divertor leg from a slab geometry. The geometry is shown in Fig. 3(a). The fixed (toroidally symmetric) background plasma state, which is typical for the high recycling regime, is plotted in Figs. 3(b)-3(d). The magnetic pitch, which is the ratio of the poloidal (θ) component and the total magnetic field, is 0.075 in the whole domain.

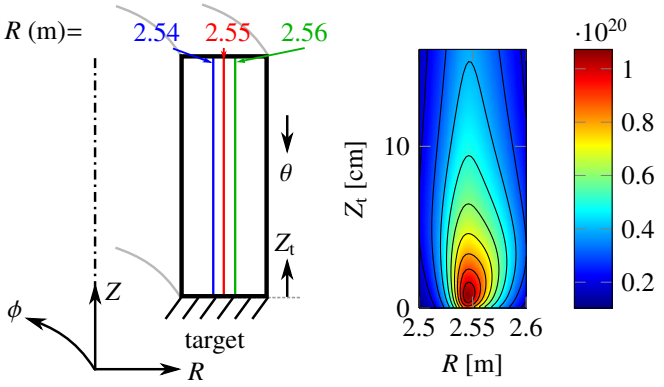

(a) Sketch of the domain.

(b) Ion = electron density (m^{-3}). Contour lines: $2, 3, \ldots, 10 \cdot 10^{19}$ m^{-3}.

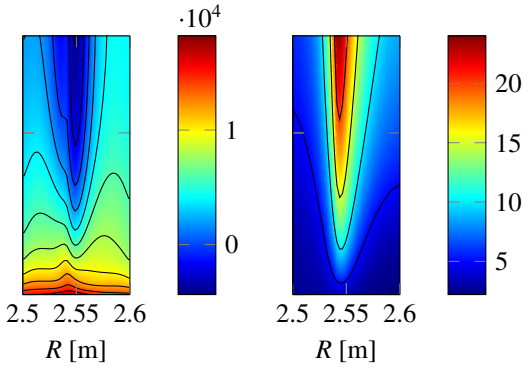

(c) Plasma parallel velocity (m/s). Contour lines: $-2, -1, \ldots, 16 \cdot 10^3$ m/s.

(d) Ion = electron temperature (eV). Contour lines: $5, 10, \ldots, 20$ eV.

Figure 3: Geometry and background plasma.

There are four boundaries: the divertor target ($Z_t = 0$ m), the upstream boundary ($Z_t = 0.5$ m), the private flux boundary ($R = 2.5$ m) and the wall boundary ($R = 2.6$ m). The magnetic field is aligned to the private flux and wall boundaries and we assume that there is no sheath acceleration for these field-aligned boundaries ($\delta_{\text{sh}}^{\text{pot}} = 0$ in Eq. (87)). For the upstream and target boundaries, we take $\delta_{\text{sh}}^{\text{pot}} = 3.1$. The recycling and reflection coefficient, respectively R^{i} and R^{n} in Eq. (35), are everywhere 1, except at the upstream

boundary with $R^{\mathrm{n}} = R^{\mathrm{i}} = 0$ and at the private flux boundary with $R^{\mathrm{n}} = 0.9$. The latter coefficient accounts for neutral pumping losses. As mentioned in Section 5.3, we use the TRIM database for the reflection kernel ($R(\mathbf{r}_{\mathrm{b}}; \mathbf{v}' \rightarrow \mathbf{v})$ in Eq. (35)). All boundaries are made of carbon. The TRIM database also tabulates the probability of fast reflection. The non-fast reflected particles are emitted as thermally released molecules. However, for this simple test case, we assume that these molecules dissociate immediately by means of Franck-Condon dissociation. The dissociated atoms are emitted isotropically with an energy of 2 eV.

The grid consists of 50 cells in the poloidal (θ) direction, with an exponential refinement towards the target plate (widths of cells adjacent to the upstream and target boundary are respectively 2.85 and 0.19 cm). In the radial (R) direction, the grid consists of 40 equidistant cells. No under-relaxation or false-time stepping is needed to converge the pure fluid models (no kinetic corrections) without energy equation (models 1-2), i.e., $\alpha = 1$ and $\Delta t = \infty$. This is different for the model with energy equation (model 3) where we take $\alpha = 0.5$ and $\Delta t = 10^{-5}$ s. These relaxation factors and time steps are also used for the hybrid simulations. It should be noted that these numerical parameters are case dependent. As future research, it is interesting to perform a detailed stability analysis w.r.t. the different parameters in the equations. The MC simulation of the full kinetic equation is performed with 10^6 particles. For the hybrid simulations, we use 10^6 particles for both the positive and negative stratum for each iteration, and start the iteration procedure from the converged pure fluid neutral solution.

In Section 7.3, we show the resulting plasma sources from the different models in some relevant flux tubes to obtain a quantitative assessment of the different models. For a slab geometry, this means that we plot the plasma sources as a function of the distance to the target Z_{t} at fixed radial distances. The flux tubes with their radial locations are indicated in Fig. 3(a). The colors of the plasma sources in Section 7.3 correspond to the colors of the flux tubes in Fig. 3(a).

7.2. Evalutation of the balances for the solved fluid moments

When a steady-state solution is reached, the residual $R_i(\Phi^n)$, defined in Eq. (96), converges to machine accuracy. A finite-volume discretization of the macro part ensures a conservation of the solved fluid moments. This means that in steady-state following balance equation is fulfilled:

$$B(\Phi^n) = \left| \frac{1}{\sum_{i=1}^{N_{\mathrm{D}}} |\Phi_i^n \mathcal{V}_i|} \left(\sum_{i=1}^{N_{\mathrm{D}}} S_i(\Phi^n) - \sum_{j=1}^{N_{\mathrm{b}}} F_j(\Phi^n) \right) \right| = 0, \tag{106}$$

with $S_i(\Phi^n)$ the source in cell i and $F_j(\Phi^n)$ the outgoing boundary flux at face j. Although, $B(\Phi^n)$ reaches machine accuracy for the pure fluid models, i.e., the solutions of the macro equations of Section 3.2 without kinetic contributions, this is not the case for the hybrid models due to the presence of the statistical noise. However, following balance equation is fulfilled for every iteration for both the fluid and hybrid simulations:

$$C(\Phi^n) = \left| \frac{1}{\sum_{i=1}^{N_{\mathrm{D}}} |\Phi_i^n \mathcal{V}_i|} \left(\sum_{i=1}^{N_{\mathrm{D}}} \left(S_i(\Phi^{n-1}) + \frac{\partial S_i}{\partial \Phi}(\Phi^{n-1}) \Delta \Phi^n \right) - \sum_{j=1}^{N_{\mathrm{b}}} \left(F_j(\Phi^{n-1}) + \frac{\partial F_j}{\partial \Phi}(\Phi^{n-1}) \Delta \Phi^n \right) - \sum_{i=1}^{N_{\mathrm{D}}} \frac{\Delta \Phi_i^n}{\Delta t} \mathcal{V}_i \right) \right| = 0, \tag{107}$$

which means that there is a balance for the linearized sources and fluxes. Fig. 4 shows $B(\Phi^n)$ and $C(\Phi^n)$ as a function of the iteration number for both pure fluid and hybrid simulations for the most advanced model with energy equation (model 3). This proves the fact that the micro-macro scheme is conservative.

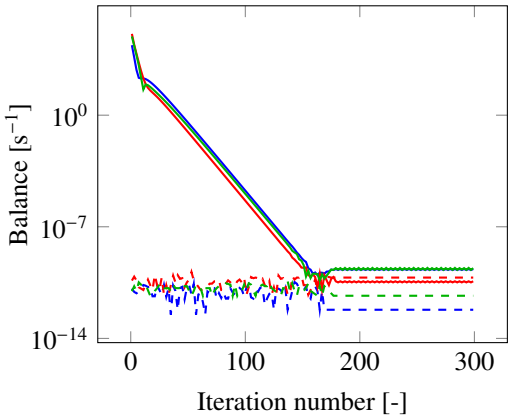

(a) Pure fluid simulations.

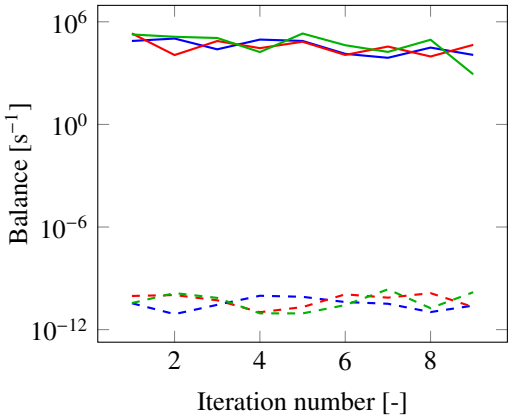

(b) Hybrid simulations.

Figure 4: Balances as a function of the iteration number: continuity (blue), momentum (red) and energy (green). The solid and dashed lines represent respectively $B(\Phi^n)$ (Eq. (106)) and $C(\Phi^n)$ (Eq. (107)).

7.3. Plasma sources

Figs. 5-7 show the results for respectively the particle, parallel momentum and ion energy source in the selected flux tubes. For the momentum and energy source, we only show the results in the red flux tube at $R = 2.55$ m where these sources peak. The results in the other flux tubes are qualitatively the same. Besides the hybrid solutions with kinetic corrections averaged over a high number of iterations to obtain a negligible statistical error on the final result, we also plot the deterministic fluid solutions.

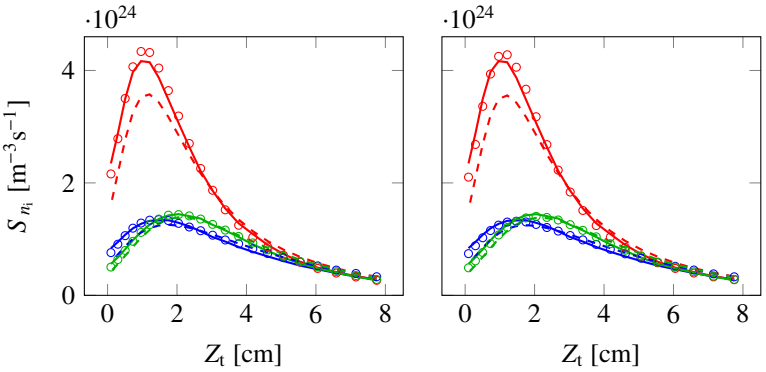

(a) Pure pressure-diffusion equation (model 1).

(b) Continuity and parallel momentum equation (model 2).

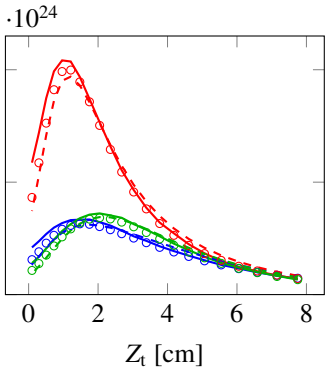

(c) Continuity, parallel momentum and energy equation (model 3).

Figure 5: Particle source in selected flux tubes: full kinetic MC solution (solid line), solution of the pure fluid model (dashed line) and hybrid solution (circles). The colors correspond to the location of the flux tubes, as indicated in Fig. 3(a).

Although the hybrid method in general succeeds to correct for the fluid errors, there are some remaining hybrid-kinetic discrepancies. After averaging the solution over a high number of iterations, the discretization error, finite-sampling bias and convergence error are the only remaining numerical errors. In Ref. [28], we show that the hybrid errors for the pure pressure-diffusion model (model 1, left hand side of Figs. 5-7) are mainly caused by the discretization error. In Fig. 8, we illustrate this again for the momentum and energy source by performing a grid refinement. The MC solution is almost not influenced by the grid refinement. Hence, we only show the full kinetic MC results on the 50×40 grid. The hybrid-kinetic discrepancies are much smaller for the model with parallel momentum equation and ion-neutral thermal equilibrium (model 2, middle of Figs. 5-7). For the model with energy equation (model 3, right hand side of Figs. 5-7), there is a large remaining hybrid error for the ion energy source (see Fig. 7(c)). To verify if this error is of numerical nature, we compare simulation

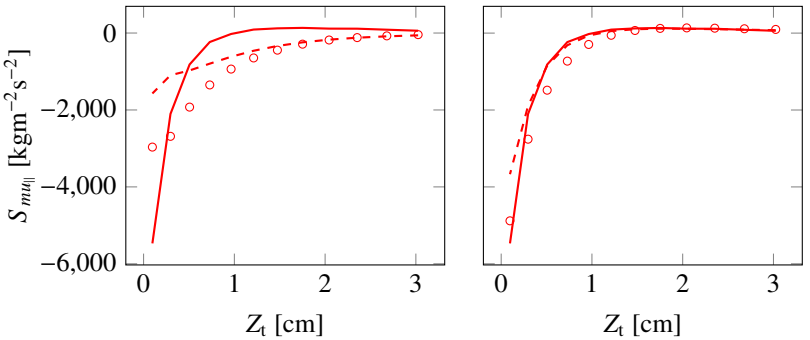

(a) Pure pressure-diffusion equation (model 1).

(b) Continuity and parallel momentum equation (model 2).

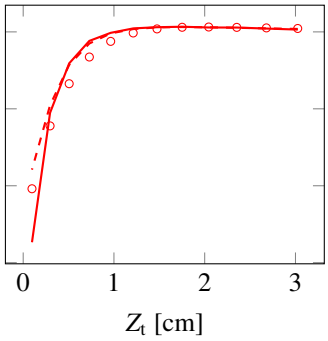

(c) Continuity, parallel momentum and energy equation (model 3).

Figure 6: Parallel momentum source in red flux tube at $R = 2.55$ m (see Fig. 3(a)): full kinetic MC solution (solid line), solution of the pure fluid model (dashed line) and hybrid solution (circles).

results with different amounts of particles and on two grids.

According to Ref. [7], the sum of the finite-sampling bias and convergence error, which we bluntly call the bias, is approximately inversely proportional to the number of MC particles. Hence, if there is still a significant remaining bias for the hybrid result in Fig. 7(c), then a variation of the number of particles should lead to a change in ion energy profile. As can be seen in Fig. 9(a), this is definitely not the case and we can conclude that the bias is not the cause for the hybrid-kinetic discrepancy in Fig. 7(c).

To estimate the discretization error, we perform the hybrid simulation on two different grids. Fig. 9(b) shows the results. Again, the differences for the results on both grids are much smaller than the hybrid-kinetic discrepancy in Fig. 7(c). Hence, also the discretization error is not the reason for the hybrid error.

From this analysis, we can conclude that the hybrid-kinetic discrepancy in Fig. 7(c) is caused by a modeling error. By assuming a perfect drifting Maxwellian for the fluid neutral distribution (see Eq. (34)), the hybrid model is not completely equivalent to the kinetic equation. This issue is expected to disappear when using a fluid neutral

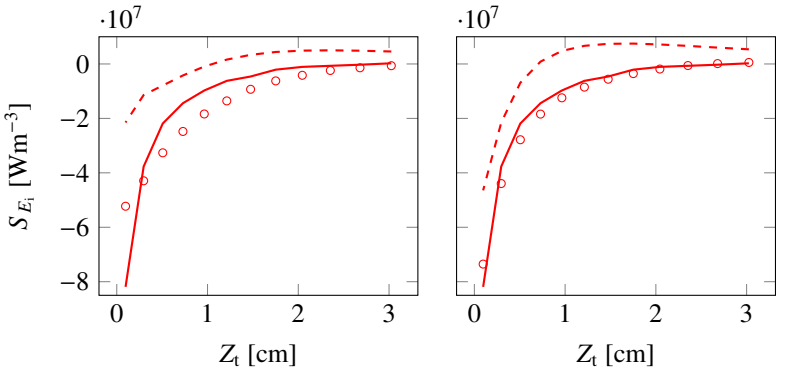

(a) Pure pressure-diffusion equation (model 1).

(b) Continuity and parallel momentum equation (model 2).

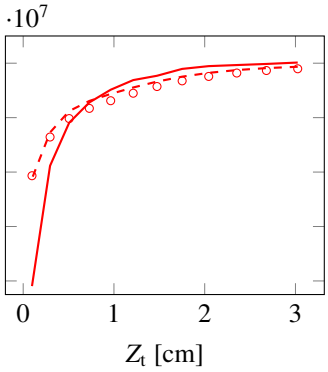

(c) Continuity, parallel momentum and energy equation (model 3).

Figure 7: Ion energy source in red flux tube at $R = 2.55$ m (see Fig. 3(a)): full kinetic MC solution (solid line), solution of the pure fluid model (dashed line) and hybrid solution (circles).

distribution that exactly corresponds to the selected fluid model. A possible solution is the use of Grad's series expansion with Hermite polynomials for $f_{\mathrm{n,f}}(\mathbf{r}, \mathbf{v})$ to take into account the viscous momentum and conductive heat transport [40]. We can conclude that the use of a hybrid approach without an exact fluid neutral distribution expression is here not recommended for model 3, as it only gives minor changes compared to the pure fluid solution.

7.4. CPU time reduction

The objective of the hybrid approach is to reduce the CPU time compared to an MC simulation of the full kinetic equation for the same statistical error on a certain quantity of interest. We are mainly interested in the plasma sources and we define the statistical

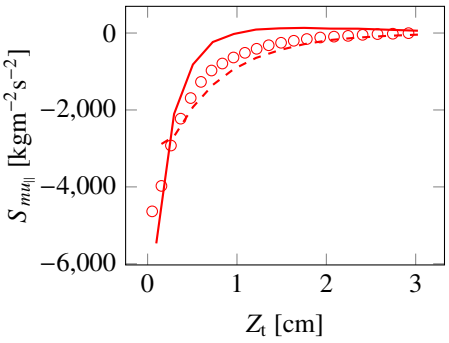

(a) Parallel momentum source.

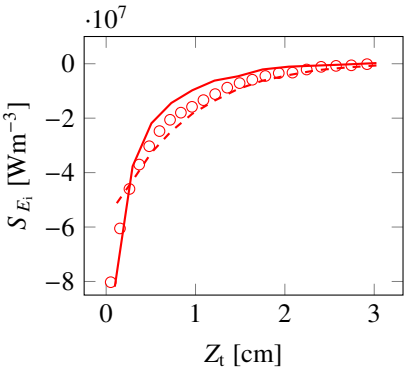

(b) Ion energy source.

Figure 8: Grid refinement for the hybrid model with pure pressure-diffusion equation (model 1): full kinetic MC solution on 50×40 grid (solid line), hybrid solution on 50×40 grid (dashed line) and on 100×80 grid (circles). The results are plotted for the red flux tube, as indicated in Fig. 3(a).

error $\epsilon_{s,S}$ on an arbitrary source S (particle, momentum or energy) as

$$\epsilon_{s,S} = \sqrt{\sum_{i=1}^{N_D} \sigma_{S,i}^2}, \tag{108}$$

with $\sigma_{S,i}$ the local value of the standard deviation in the center of cell i. The statistical error of an MC simulation of the full kinetic equation (subscript K) can be approximated as $\epsilon_{s,S,K} \approx A_{S,K}/\sqrt{CPU_K}$, with CPU_K the CPU time and $A_{S,K}$ a scaling coefficient. This scaling law follows from the typical $1/\sqrt{N}$ statistical error scaling and the assumption that $CPU_K \sim N$. According to Ref. [7], the statistical error for a coupled finite-volume–MC simulation with averaging over I iterations scales with $1/\sqrt{NI}$. We assume that the CPU time for the hybrid simulation (subscript H) scales as $CPU_H \sim NI$. This scaling becomes valid when the cost of the fluid part and the transient phase becomes negligible. Indeed, if we start from the pure fluid solution, we can start averaging after a few iterations. Hence, the hybrid statistical error can be

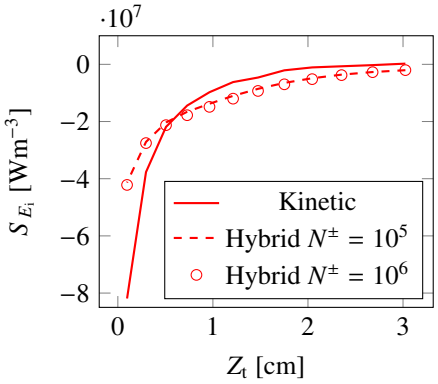

(a) Different amounts of particles (50×40 grid).

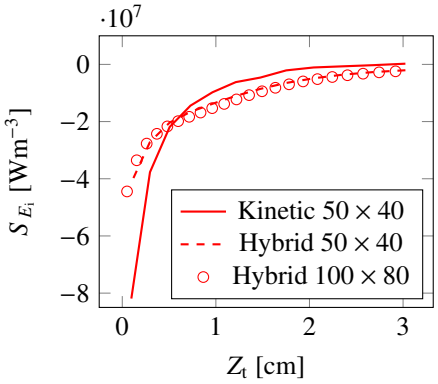

(b) Two grids ($N^{\pm} = 10^6$ particles).

Figure 9: Ion energy source in red flux tube indicated in Fig. 3(a) from model with energy equation (model 3) when varying the particle amount and grid size.

approximated as $\epsilon_{s,S,\mathrm{H}} \approx A_{S,\mathrm{H}}/\sqrt{CPU_{\mathrm{H}}}$, and the ratio of the kinetic and hybrid CPU time becomes

$$\frac{CPU_{\mathrm{K}}}{CPU_{\mathrm{H}}} \approx \left(\frac{A_{S,\mathrm{K}}}{A_{S,\mathrm{H}}}\right)^2 . \tag{109}$$

Table 2 tabulates this ratio for the different models.

The pure pressure-diffusion model (1) is only able to slightly reduce the CPU time for the same particle source statistical error, but the model is much slower for the other sources. Due to large inaccuracies for the momentum and energy source from the pure fluid solution (see left hand side of Figs. 6-7), the kinetic contribution becomes too large to reduce the overall statistical error. A parallel momentum equation has to be added to reduce the CPU time for the same momentum and energy source statistical errors. Finally, the model with energy equation (3) clearly outperforms the other models with respect to the statistical error reduction. However, it should be kept in mind that the accuracy of model 3 for the ion energy source is still unsatisfactory (see Fig. 7(c)).

Table 2: Ratio of CPU time of kinetic and hybrid simulations for the same statistical error on a certain source ($CPU_{\mathrm{K}}/CPU_{\mathrm{H}}$) for the different hybrid models.

	Particle source	Parallel momentum source	Ion energy source
Pure pressure-diffusion equation (model 1)	1.08	0.32	0.90
Continuity and parallel momentum equation (model 2)	1.35	5.81	1.99
Continuity, parallel momentum and energy equation (model 3)	5.34	27.56	23.91

Finally, we mention that simulations with pure fluid neutral models are at least an order of magnitude faster than the kinetic MC simulations with a minimum number of particles to reach a statistically stationary state when solving the coupled fluid plasma – kinetic neutral equations. Pure fluid simulations are extremely useful for preliminary fast parameter scans.

8. Conclusions and future work

We tested the micro-macro decomposition method of the kinetic equation for the plasma edge atoms. We considered three macro/fluid models: (i) a pure pressure-diffusion equation assuming equal ion and neutral temperatures; (ii) a continuity and parallel momentum equation with pressure-diffusion transport only retained in the directions perpendicular to the magnetic field lines, again with identical ion and neutral temperatures; and (iii) the same as (ii), but with a separate neutral energy equation, i.e., we no longer assume equal ion and neutral temperatures. By assuming a perfect drifting Maxwellian for the fluid neutral distribution, we introduced a modeling error compared to the full kinetic equation. Although the hybrid-kinetic discrepancies for the plasma sources for the models without energy equation remain limited, there is a significant remaining error for the ion energy source for the model with energy equation.

We have assessed the performance of the hybrid models on the basis of the CPU time reduction compared to an MC simulation of the full kinetic equation for the same statistical error on a certain source. We conclude that the accuracy of the underlying fluid model is of crucial importance to substantially reduce the CPU time. Consequently, the inaccurate pressure-diffusion model is not able to reduce the CPU time regarding the parallel momentum and ion energy source statistical error. The model with energy equation and including a projection step after each micro iteration gives the largest CPU time reductions, i.e., approximately a factor of 5, 28 and 24 for respectively the particle, parallel momentum and ion energy source statistical error.

As further research, the performance of the hybrid models has to be evaluated for coupled plasma-neutral simulations. Besides that, the hybrid approach has to be assessed for cases that include more extended physics. E.g., neutral-neutral collisions have to be incorporated for high-density plasma simulations. It is expected that it is much easier to handle these nonlinear neutral self-collisions with a (partially) macroscopic model instead of with a full kinetic approach. The mono-species simulation

has to be extended towards multiple species (both atoms and molecules). The safest option is to exclusively use the hybrid approach for the deuterium atoms. However, (partially) deterministic models for the other species could further reduce the MC calculation time. Especially, the CPU share of the deuterium molecules is significant and a (partially) deterministic model might be beneficial.

Acknowledgments

The work of N. Horsten is supported by a PhD grant of the Research Foundation Flanders (FWO Vlaanderen). Parts of the work are supported by the Research Foundation Flanders (FWO) under project grant G078316N.

References

[1] W. Fundamenski, Power exhaust in fusion plasmas, Cambridge University Press, 2010.

[2] S. Braginskii, Transport processes in a plasma, Reviews of plasma physics 1 (1965) 205.

[3] A. Wootton, B. Carreras, H. Matsumoto, K. McGuire, W. Peebles, C. P. Ritz, P. Terry, S. Zweben, Fluctuations and anomalous transport in tokamaks, Physics of Fluids B: Plasma Physics 2 (1990) 2879–2903.

[4] D. Reiter, The data file AMJUEL: Additional atomic and molecular data for EIRENE, Technical Report, FZ Juelich, 2000.

[5] D. Reiter, The Data File HYDHEL: Atomic and Molecular Data for EIRENE, Technical Report, FZ Juelich, 2002.

[6] D. Reiter, M. Baelmans, P. Börner, The EIRENE and B2-EIRENE codes, Fusion Science and Technology 47 (2005) 172–186.

[7] K. Ghoos, W. Dekeyser, G. Samaey, P. Börner, M. Baelmans, Accuracy and Convergence of Coupled Finite-volume/Monte Carlo Codes for Plasma Edge Simulations of Nuclear Fusion Reactors, Journal of Computational Physics 322 (2016) 162–182.

[8] S. Jin, Efficient asymptotic-preserving (AP) schemes for some multiscale kinetic equations, SIAM Journal on Scientific Computing 21 (1999) 441–454.

[9] N. Horsten, G. Samaey, M. Baelmans, Development and assessment of 2D fluid neutral models that include atomic databases and a microscopic reflection model, Nuclear Fusion 57 (2017) 116043.

[10] Q. Sun, I. D. Boyd, G. V. Candler, A hybrid continuum/particle approach for modeling subsonic, rarefied gas flows, Journal of Computational Physics 194 (2004) 256–277.

[11] D. Y. Anistratov, N. D. Stehle, Computational transport methodology based on decomposition of a problem domain into transport and diffusive subdomains, Journal of Computational Physics 231 (2012) 8009–8028.

[12] N. Crouseilles, P. Degond, M. Lemou, A hybrid kinetic/fluid model for solving the gas dynamics Boltzmann–BGK equation, Journal of Computational Physics 199 (2004) 776–808.

[13] G. Dimarco, L. Pareschi, Hybrid multiscale methods II. Kinetic equations, Multiscale Modeling & Simulation 6 (2008) 1169–1197.

[14] A. Klar, An asymptotic-induced scheme for nonstationary transport equations in the diffusive limit, SIAM journal on numerical analysis 35 (1998) 1073–1094.

[15] C. Buet, S. Cordier, An asymptotic preserving scheme for hydrodynamics radiative transfer models, Numerische Mathematik 108 (2007) 199–221.

[16] M. Bennoune, M. Lemou, L. Mieussens, Uniformly stable numerical schemes for the Boltzmann equation preserving the compressible Navier–Stokes asymptotics, Journal of Computational Physics 227 (2008) 3781–3803.

[17] M. Lemou, L. Mieussens, A new asymptotic preserving scheme based on micro-macro formulation for linear kinetic equations in the diffusion limit, SIAM Journal on Scientific Computing 31 (2008) 334–368.

[18] N. Crouseilles, M. Lemou, An asymptotic preserving scheme based on a micro-macro decomposition for collisional Vlasov equations: diffusion and high-field scaling limits., Kinetic and Related Models 4 (2011) 441–477.

[19] S. Boscarino, L. Pareschi, G. Russo, Implicit-explicit Runge–Kutta schemes for hyperbolic systems and kinetic equations in the diffusion limit, SIAM Journal on Scientific Computing 35 (2013) A22–A51.

[20] A. Crestetto, N. Crouseilles, M. Lemou, Kinetic/fluid micro-macro numerical schemes for Vlasov-Poisson-BGK equation using particles, Kinetic and Related Models 5 (2012) 787–816.

[21] A. Crestetto, N. Crouseilles, M. Lemou, A particle micro-macro decomposition based numerical scheme for collisional kinetic equations in the diffusion scaling, Communications in Mathematical Sciences 16 (2018) 887–911.

[22] G. Dimarco, L. Pareschi, G. Samaey, Asymptotic-Preserving Monte Carlo methods for transport equations in the diffusive limit, SIAM Journal on Scientific Computing 40 (2018) A504–A528.

[23] C. Karney, D. Stotler, B. Braams, Modeling of neutral plasma in a divertor in the fluid-kinetic transition, Contributions to Plasma Physics 38 (1998) 319–324.

[24] M. Valentinuzzi, Y. Marandet, H. Bufferand, G. Ciraolo, P. Tamain, Two-phases hybrid model for neutrals, Nuclear Materials and Energy 18 (2019) 41–45.

[25] I. M. Gamba, S. Jin, L. Liu, Micro-macro decomposition based asymptotic-preserving numerical schemes and numerical moments conservation for collisional nonlinear kinetic equations, Journal of Computational Physics 382 (2019) 264–290.

[26] A. Kukushkin, H. Pacher, V. Kotov, D. Reiter, D. Coster, G. Pacher, Effect of conditions for gas recirculation on divertor operation in ITER, Nuclear Fusion 47 (2007) 698.

[27] N. Horsten, G. Samaey, M. Baelmans, Hybrid fluid–kinetic neutral model based on a kinetic correction on a fluid solution, Contributions to Plasma Physics 58 (2018) 703–709.

[28] N. Horsten, G. Samaey, M. Baelmans, Hybrid fluid-kinetic model for neutral particles in the plasma edge, Nuclear Materials and Energy 18 (2019) 201–207.

[29] R. J. Goldston, P. H. Rutherford, Introduction to plasma physics, CRC Press, 1995.

[30] V. Rozhansky, S. Voskoboynikov, E. Kaveeva, D. Coster, R. Schneider, Simulation of tokamak edge plasma including self-consistent electric fields, Nuclear Fusion 41 (2001) 387.

[31] D. Reiter, The EIRENE code user manual, 2009.

[32] A. Bobylev, The Chapman-Enskog and Grad methods for solving the Boltzmann equation, in: Proceedings of Akademiia Nauk SSSR Doklady, volume 262, 1982, pp. 71–75.

[33] S. Wiesen, D. Reiter, V. Kotov, M. Baelmans, W. Dekeyser, A. Kukushkin, S. Lisgo, R. Pitts, V. Rozhansky, G. Saibene, et al., The new SOLPS-ITER code package, Journal of Nuclear Materials 463 (2015) 480–484.

[34] M. Junk, Domain of definition of Levermore's five-moment system, Journal of Statistical Physics 93 (1998) 1143–1167.

[35] P. Stangeby, Plasma sheath transmission factors for tokamak edge plasmas, The Physics of fluids 27 (1984) 682–690.

[36] P. W. Glynn, D. L. Iglehart, Importance sampling for stochastic simulations, Management Science 35 (1989) 1367–1392.

[37] B. Mortier, M. Baelmans, G. Samaey, An analytical study of Monte Carlo source term estimators in plasma edge simulations of fusion reactors, in: Proceedings of International Conference on Mathematics & Computational Methods Applied to Nuclear Science & Engineering, 2017.

[38] G. Fishman, Monte Carlo: concepts, algorithms, and applications, Springer Science & Business Media, 2013.

[39] J. S. Liu, Monte Carlo strategies in scientific computing, Springer Science & Business Media, 2008.

[40] H. Grad, On the kinetic theory of rarefied gases, Communications on pure and applied mathematics 2 (1949) 331–407.